8-15-2016

Testing the Sea Level Hypothesis with New Records along the Southern East Pacific Rise and Pacific Antarctic Ridge

Emily I. Seeley
University of Connecticut, emily.seeley@uconn.edu

Testing the Sea Level Hypothesis with New Records along the Southern East Pacific Rise and Pacific Antarctic Ridge

Emily Irene Seeley

B.S., University of Michigan, 2013

A Thesis

Submitted in Partial Fulfillment of the

Requirements for the Degree of

Master of Science

At the

University of Connecticut

2016

APPROVAL PAGE

Masters of Science Thesis

Testing the Sea Level Hypothesis with New Records along the Southern East Pacific Rise and Pacific Antarctic Ridge

Presented by

Emily Irene Seeley, B.S.

Major Advisor_____

David C. Lund

Associate Advisor_____

Penny Vlahos

Associate Advisor_____

Robert Mason

University of Connecticut

2016

ACKNOWLEDGMENTS

Although my name appears at the top of this thesis, I am by no means the sole contributor. Without the knowledge, time, and assistance of those thanked below, this thesis may have never have come to fruition.

I am very grateful to my advisor, David Lund, for presenting me with the opportunity to complete my Masters at the University of Connecticut, as well as my initial exposure to the field of Oceanography. I would never have made the trip to UConn without his guidance and support. His expertise in the field of paleoceanography has been invaluable to me. I thank him for his patience, encouragement, and for allowing me to interrupt many a lunch to work through my latest setback or to celebrate a recent achievement. Without his countless suggestions, explanations, and edits, this thesis would not be what it is today.

I would also like to thank my committee members, Penny Vlahos and Rob Mason. I thank Rob for his timely assistance and input regarding my methods development, without which may have delayed my progress by many more months. I also thank Penny for her constant stream of encouragement and for pushing me to explore the literature outside of the paleoclimate discipline.

The methods development of this thesis has benefitted from discussions with Jennifer Morford of Franklin & Marshall College, and Jason Demers and Jamie Gleason of the University of Michigan. I would also like to thank Jason individually for sharing his meticulous lab technique with me, which has greatly added to the success of the metal concentration data within. Additional thanks goes to Maziet Cheseby and Cara Fritz of the Oregon State University Marine Geology Repository for providing excellent photographs and log data for the in-depth

analysis of core Y71-07-53. A special thank you to the following former and current faculty and staff at the University of Connecticut (Avery Point) for their various forms of support during my graduate study – Claudia Koerting, Pat Evans, Debra Schuler, Janet Laflamme, and Todd Fake.

Additionally, my ICP methods development and analysis would not have been possible without the knowledge and assistance of David Cady. I also would like to thank Sarah McCart for her untiring assistance with sediment digestions and other lab activities asked of her. Thank you to my proofreaders, Melissa Cote and Lija Treibergs, for their helpful critiques of my thesis. Also, thank you to Aaron Rosenberg for your time-saving Matlab scripts.

Of course, I am grateful for the support of my parents. Although this field of science is significantly outside of their comfort zone, I appreciate their encouraging words when my progress seemed to be moving backwards. I would not have gotten through this year without Trevor Prophet. His unwavering mental, physical, and emotional support has lifted me when finishing this thesis seemed impossible. While the least science-savvy of all, but with the most unconditional love, I thank my sweet pup, Pepper. I owe her so many long walks!

Finally, I appreciate the financial support from the University of Connecticut that funded parts of the research discussed in this thesis.

TABLE OF CONTENTS

LIST OF FIGURES

LIST OF TABLES

Table Page

ABSTRACT

Melting glaciers may have indirectly affected submarine volcanism via changes in sea level. As sea level quickly drops, the rate of pressure change increases, resulting in decompression melting in the upper mantle, increasing magmatic flux. Given that hydrothermal activity at mid-ocean ridges is driven by near-axis magmatic heat, the concentration of hydrothermal proxies in ridge crest sediments (Fe, Mn, and As) can be used to infer long-term changes in hydrothermal plume activity. Using a series of well-dated sediment cores from the East Pacific Rise (EPR), we find glacial-interglacial variations in the concentrations of Fe, Mn, and As at multiple locations, with peak concentrations occurring during glacial terminations. These results are similar to those from sites further north along the EPR, suggesting widespread changes in hydrothermal activity along the EPR. A basaltic ash layer in Core OC170-026-159 aligns with Glacial Termination II, suggesting a volatile, submarine eruption. Diagenetic overprinting, sediment focusing, and dilution with non-hydrothermal components are unlikely complicating factors for the interpretation of hydrothermal proxies. The release of carbon and geothermal heat during increased hydrothermal activity would promote deglaciations, but the exact mechanism remains unclear.

1. Introduction

The Pleistocene Ice Ages are characterized by the growth and decay of large continental ice sheets, which caused eustatic sea level to vary by approximately 100 m (Bard, Hamelin, and Fairbanks, 1990; Fairbanks et al., 2005). Pleistocene ice sheets contained up to ~5 x 10^{19} kg of water, which is transferred between continents and ocean basins on the time scale of approximately 10,000 years (Tushingham and Peltier, 1991). Melting ice sheets and the associated pressure release on land may have triggered an increase in Northern Hemisphere sub-aerial volcanism during the last deglaciation (Gardeweg, Sparks, and Matthews, 1998; Jellinek, Manga, and Saar, 2004; Huybers and Langmuir, 2009). For example, the retreat of ice sheets in Iceland are believed to have driven a 10x increase in volcanism during Termination I (Sigvaldason, Annertz, and Nilson, 1992; Jull and McKenzie, 1996; Maclennan et al., 2002). Similarly, pressure changes associated with global changes in sea level may influence magmatism at mid-ocean ridges. When sea level drops rapidly, the rate of decompression of the upper mantle increases, driving increased melt production in the upper mantle (Huybers and Langmuir, 2009; Lund and Asimow, 2011). As a result, we predict that glacial-interglacial changes in sea level should influence mid-ocean ridge magmatism.

There are three main steps to melt extraction at mid-ocean ridges, including 1) sub-vertical, buoyancy-driven migration of the melt in the asthenosphere, 2) focusing of melt along the high permeability barrier along the base of the lithosphere, and 3) tectonically-controlled extraction as melt moves along the plate boundary and emerges at the ridge crest (Gregg et al., 2012). The mean depth of the melt production in the asthenosphere is approximately 50 km (Key et al., 2013) and the melt migration rate is estimated to be 1-50 m/kyr. The minimum melt

migration rate is constrained by the $^{230}Th/^{238}U$ disequilibrium age in zero-age, mid-ocean ridge basalts (MORB), whose $(^{230}Th)/(^{238}U)$ ratios that are greater than one diverge from secular equilibrium (Richard and McKenzie, 1994). If the initial separation between ^{238}U and ^{230}Th happens only in the garnet peridotite stability field (>75 km depth) (Keleman et al., 1997), melt must migrate to the seafloor faster than the half-life of ^{230}Th (~75kyr), giving a minimum melt migration rate of >1 m/yr. On the other hand, the lag between deglaciation and volcanism in Iceland suggests melt migration rates may exceed 50 m/yr (Maclennan et al., 2002). The large range of melt migration velocities and mean depth of melt production imply that it takes between ~1 kyr to 50 kyr for melt to arrive at the ridge crest. Therefore, any changes in melt production will likely reach the ridge crest thousands of years after the initial sea level forcing (Lund and Asimow, 2011). Hydrothermal records from the East Pacific Rise (EPR) imply melt migration rates between 2.5-5 m/yr (Lund et al., 2016). These estimates were determined by dividing the average melt depth origin (~50 km, Key et al., 2013) by the time elapsed between the maximum rate of sea level decrease and the maximum hydrothermal metal flux or concentration. Because of the lag, we predict that changes in sea-level should lead proxies of mid-ocean ridge magmatism at the EPR over glacial-interglacial timescales.

Although sea level driven changes in upper mantle melt production likely occur, the expression of the resulting magmatic signal at the seafloor, if any, remains unclear. One idea is that changes in melt production may be recorded in the fabric of abyssal hills, which appear to have a spacing similar to Milankovitch periods (Lund and Asimow, 2011; Crowley et al., 2015; Tolstoy, 2015). Olive et al. (2015) combined classic seafloor observations with a model of mid-ocean ridge dynamics to demonstrate whether oscillations in melt supply of a given period (τ)

can imprint seafloor bathymetry using three mechanisms: 1) static topographic compensation, 2) volcanic extrusion on the seafloor, and 3) interactions between tectonic plates and magmatic activity during normal fault growth. The simulations suggest that all three seafloor-shaping processes act as a low-pass filter on variations in magma supply, strongly damping fluctuations shorter than about 100,000 years. The results of Olive et al. (2015) call into question whether Milankovitch-scale variations in melt production can be recorded in seafloor bathymetric records. Furthermore, the limited age control for bathymetry records make it difficult to determine the exact timing of melt anomalies at the seafloor, which is essential to understanding whether anomalous magmatism influences the climate system. Given these issues, additional proxies for magmatism at mid-ocean ridge are necessary for evaluating the sea level hypothesis.

Here, we take a different approach and use proxies of hydrothermal activity at mid-ocean ridges. Hydrothermal activity occurs in three main stages. First, hydrothermal fluids are formed upon seawater entering the vent system, where the seawater is heated as it reacts with molten basalt. The resulting O_2-poor, acidic hydrothermal fluid rises through the oceanic crust and encounters cold, O_2-rich bottom water, creating various forms of iron sulfide, iron hydroxide and manganese oxide particles (Lilley et al., 1995; Millero, 2013). Then, the plume rises until its density is equal to that of the surrounding seawater and reaches neutral buoyancy (~200-400 m). Finally, it spreads laterally and Fe oxyhydroxides (FeOOH) and Mn oxides (MnO_2) precipitate, scavenges trace metals such as As and from the surrounding seawater, and travels tens of kilometers from the system (Feely et al., 1992). Typically, the plume stays within 100 km or less of the ridge crest (Dymond, 1981). The material in the neutrally buoyant plume eventually

settles out of the plume leaving Fe and Mn-rich metalliferous deposits on the ridge flanks (Lilley et al., 1995; German et al., 2002; Millero, 2013).

A global compilation of hydrothermal plume observations suggests that hydrothermal plume incidence (the fraction of ridge overlain by a plume) scales linearly with the magmatic budget for a given ridge section (Baker, Chen, and Phipps Morgan, 1996). Because of its high magmatic budget, the SEPR has the highest known plume incidence of any ridge on Earth, among over 50 known active hydrothermal vent sites from 5°S to 37°S (Beaulieu et al., 2013). Thus, the SEPR is an ideal region for reconstructing plume activity in the geologic past because it is densely populated with hydrothermal vent systems, providing comprehensive spatial and temporal coverage of magmatic activity at the ridge crest. Baker et al. (2009) conducted a more quantitative measure of plume intensity and axial magma chamber (AMC) incidence and depth at six ridges, including 14-18.5°S along the southern East Pacific Rise (SEPR). Results from the SEPR show a relatively linear relationship between plume incidence and AMC presence (Baker and German, 2004; Baker, 2009). Therefore, enhanced magmatic output should yield more intense plume activity, which we can monitor by using metalliferous sediments.

Sediment cores are a geological archive whose metal concentrations can be measured to infer hydrothermal activity. Initial studies of the SEPR surveyed the top 5-10 cm of sediment cores (core tops) from 0° to 40°S, spanning the width of the Nazca Plate to the east and extending out almost 1000 km to the west of the EPR (Dymond, 1981). Core top sediments within 100 km of the EPR are highly enriched in hydrothermal Fe and Mn precipitates and scavenged elements, with an Fe/Mn weight percentage ratio of approximately 3.5 ± 0.9 (1σ) (Böstrom et al., 1969; Dymond, 1981). Subsequent studies of EPR ridge crest sediment have

found similar down core Fe/Mn ratios, implying that it can be used as a semi-quantitative diagnostic indicator of hydrothermal input (Metz, Trefry, and Nelsen, 1988; Shimmield and Price, 1988; Frank et al., 1994; Schaller et al., 2000; Dunk and Mills, 2006; Mills et al., 2010; Lund et al., 2016).

A recent study (Lund et al., 2016) developed nine hydrothermal records with age control along the EPR, including two cores at 1°N (near the East Pacific Rise-Dietz volcanic triple junction) (Frank et al., 1994), three cores at 5-6°S (Lund et al., 2016), and four cores at 10-11°S (Schaller et al., 2000; Lund et al., 2016). The study generally finds Fe/Mn ratios of ~3.5, with Fe, Mn, and As concentrations coherently peaking during Terminations I (TI) and II (TII). Metal fluxes estimated by mass accumulation rates (MARs) also record contemporaneous maxima during TI. Fluxes were cross-checked using the ^{3}He normalization method; at both 6°S and 11°S, the ^{3}He-based results confirm the MAR estimates. Overall, the nine cores show a similar pattern in hydrothermal metal fluxes along 1300 km of the EPR, regardless of whether they were determined by MAR or ^{3}He-based methods.

Factors in addition to hydrothermal activity that could influence the metal flux records include diagenesis, horizontal sediment focusing, and dilution from biogenic material. Lund et al. (2016) concluded that diagenesis is an unlikely driver of the metal patterns at 5-6°S and 10-11°S based on the agreement between down core Fe/Mn values and the hydrothermal endmember for EPR sediments. Additionally, Fe and Mn maxima co-occur in multiple cores; if diagenetic remobilization occurred, there would likely be separation of Fe and Mn maxima with depth in the cores. The one exception is at 1°N, however, where anomalously high Fe/Mn ratios

occurred prior to 20 kyr BP, most likely due to diagenetic remobilization and removal of Mn^{2+} (Lund et al., 2016). Overall, however, there is clear agreement between records from the highly productive equatorial Pacific (1°N) to the northern edge of the subtropical gyre (10-11°S). This suggests that organic carbon (C_{org}) flux to the sediments is not a first order control on down core metal variability. It is also unlikely that sediment focusing is an important factor given the similar flux pattern in multiple cores from either side of the EPR and spanning a range of sedimentary environments. Core Y71-07-49 at 11°S with ^{3}He focusing factors displays no evidence of anomalous horizontal sediment winnowing or focusing during TI (Lund et al., 2016). Additionally, these same cores with ^{3}He-based fluxes display metal patterns consistent with MAR-based fluxes, indicating that calcium carbonate ($CaCO_3$) dilution signal did not control the Fe, Mn, and As peaks in down core signals.

In order to more fully evaluate whether diagenesis could have possibly driven coherent signals across multiple core sites, this thesis develops records of hydrothermal sedimentation at 11°S, 19°S, and 39°S, spanning from the northern to the southern edge of the South Pacific subtropical gyre (Figure 1). Exact locations of the three records are listed in Table 1. At 11°S, core Y71-07-53 is located on the western flank of the SEPR, approximately 34 km from the ridge axis, where the half-spreading rate is 74 mm/year (Lund et al., 2016). The general sediment composition at 11°S is 60-80 % $CaCO_3$, 4-6 % biogenic opal, 16-24 % hydrothermal metals, and less than 8 % detrital input (Dymond, 1981). Core OC73-03-20 (19°S) also falls on the western flank of the SEPR, but is considerably closer to the ridge crest (7 km). The general sediment composition at 19°S is predominantly hydrothermal input, making up greater than 48 % of the total composition. Calcium carbonate ranges from 40-60 %, while detrital input

contributes less than 12 % and biogenic opal contribute less than 6 % (Dymond, 1981). This location has a half-spreading rate of 77 mm/year. Finally, core OC170-026-159 (15 km) falls on the western flank of the Pacific Antarctic Ridge (PAR) at 39°S, where the half-spreading rate is 49 mm/year. The general sediment composition at 39°S is similar to 11°S, with a range of 60-80 % $CaCO_3$ and less than 8 % detrital input. However, there is less biogenic opal input (< 4 %) and a greater hydrothermal metal input (16-32 %) at 39°S (Dymond, 1981). The three sites span a range of sedimentary environments, surface-ocean productivity regimes, and spreading rates.

Table 1: Name, depth, location, and distance from the ridge crest of the cores selected along the SEPR from the Nazca and Antarctic Plates.

	Core Name	Depth (m)	Latitude (°)	Longitude (°)	Distance from Ridge Crest (km)
1)	Y71-07-53	3180	-10.875	-110.730	34
2)	OC73-03-20	3081	-19.248	-113.575	7
3)	OC170-026-159	2754	-38.967	-111.350	15

In addition to measuring Fe and Mn concentrations, we also measure As, Mo, V, and Zn. Following previous studies that measure concentrations of hydrothermal plume particles in EPR sediments, we predict that these scavenged particles will vary coherently with the main Fe and Mn compounds (Morford and Emerson, 1999; Schaller et al., 2000; Cave et al., 2002; Dunk and Mills, 2006). By constructing age models for each record using oxygen stable isotope stratigraphy, we can assess the timing of change in hydrothermal sedimentation at the three sites. Our goal is to determine whether hydrothermal activity increased following significant drops in sea level during the past 150,000 years.

2. Methods

a) Age Models

SEPR core samples were collected from the Oregon State University Marine Geology Repository. Cores were initially selected based on latitude and proximity to the ridge crest (Figure 1, Table1), as sediments within 100 km of the ridge crest are unusually rich in metals due to input of hydrothermal plume particles (Dymond, 1981). Samples were frozen for a minimum of 24 hours and freeze-dried for ~48 hours. Subsamples for foraminiferal analysis were then washed over a 150 μm sieve. After washing, samples were oven-dried for ~30 minutes at 70°C and finally sorted further using a 250 μm sieve.

Oxygen stable isotope ($\delta^{18}O$) values were measured on the planktonic foraminifera *Globigerinoides ruber* (> 250 μm size fraction). Analyses were made using a Finnigan MAT253 isotope ratio mass spectrometer (IRMS) coupled to a Kiel IV automated carbonate device. Samples run at the University of Michigan Stable Isotope Laboratory (n = 54) were corrected to Vienna Pee-Dee Belemnite (VPDB) using NBS-19 (National Institute of Standards and Technology, USA) (n = 14, $\delta^{18}O$ = -2.21 ± 0.07 ‰, $\delta^{13}C$ = 1.93 ± 0.06 ‰). Samples run at Georgia Tech (n = 60) were converted to VPDB via NBS-19 (National Institute of Standards and Technology) (n = 5, $\delta^{18}O$ = -2.16 ± 0.05 ‰, $\delta^{13}C$ = 1.93 ± 0.01 ‰), NBS-18 (National Institute of Standards and Technology, USA) (n = 5, $\delta^{18}O$ = -23.12 ± 0.08 ‰, $\delta^{13}C$ = -4.91 ± 0.22 ‰), and an in-house standard with similar isotopic composition (n = 32, $\delta^{18}O$ = -2.04 ± 0.06 ‰, $\delta^{13}C$ = 2.15 ± 0.02 ‰).

Age models for cores Y71-07-53 and OC170-026-159 were determined by correlation of their planktonic $\delta^{18}O$ stratigraphy to the global benthic $\delta^{18}O$ stack of Lisiecki and Raymo (2005).

Age control points were determined based on correlation of key Marine Isotope Stage (MIS) transitions to the dated benthic stack. The approximate calendar age uncertainty for each $\delta^{18}O$ tie point is ± 3-4 kyr. Age control points were linearly interpolated to produce the final age model for each core. In the case of core OC73-03-20, we used a combination of two radiocarbon (^{14}C) control points and one $\delta^{18}O$ age control point that corresponds to the MIS 2/1 transition. The ^{14}C ages were converted to calendar ages using Calib 7.1 with the assumption of a surface water reservoir age of 400 ± 200 years (http://calib.qub.ac.uk/calib/). The typical calendar age uncertainty for each ^{14}C control point is ± 1-2 kyr. A linear interpolation of the three control points creates the final age model for OC73-03-20.

b) Sediment Digestions

Dried, ground samples underwent a four-step microwave acid digestion protocol following Morford and Emerson (1999). To ensure we had representative samples, we ground a 500 mg sample aliquot of bulk sediment from each depth rather than the 75 mg specified by Morford and Emerson (1999). A 200 mg subsample of the homogenized sediment was placed in a 60 mL, Savillex®, Teflon microwave digestion vessel and dissolved in a concentrated 5:2 HF/HNO_3 solution. The vessels were refluxed in the microwave and then evaporated to dryness. Each sample then underwent a 3:1 HCl/HNO_3 reflux and evaporation step, a 2:1 30 % H_2O_2/HNO_3 solution reflux and evaporation step, and finally a two hour reflux in 5 % HNO_3. During the method development, we found that the external standard did not completely dissolve, so we added an ~8 hour reflux to the existing HCl/HNO_3 step to complete dissolution of both standards and unknowns. The digested samples were quantitatively transferred into 125

mL Nalgene bottles and diluted up to 100 mL with 2 % HNO_3. All acids used in the digestion procedure were trace metal grade (Optima™).

c) Metal Concentrations

Bulk metal concentrations of Ca, Fe, Mn, Al, Ti, V, Cu, Zn, Ni, As, Mo, and Cr were determined using inductively-coupled plasma mass spectrometry (ICP-MS). The raw data are displayed in Tables 3 (Y71-07-53), 4 (OC73-03-20), and 5 (OC170-026-159) (see Appendix). Note that core OC170-026-159 has two values listed for 132 cm in Table 5. These are two unique digestions from two different samples. We averaged the results from the two analyses in the remaining figures and discussion.

Metal analyses were performed using a Thermo Scientific™ Element 2™ ICP-MS coupled with an ESI SC-2 DX Autosampler. We quantified elemental concentrations using standard addition of matrix-matched spike solutions. Spike solutions were gravimetrically prepared using standards from Accustandard (http://www.accustandard.com/). Spiked samples were diluted to 1/15 in 2 % HNO_3 prior to analysis. Internal spikes (^{89}Y and ^{115}In) were added to select samples in cores OC73-03-20 and OC170-026-159 to monitor quantitative transfer throughout the digestion and analysis. Digestion blanks were subtracted from each sample.

Analytical precision and accuracy were assessed through repeated digestion, measurement, and analysis of a certified standard, MESS-4 (National Research Council, Canada) (n = 22) (Table 2). For major elements (Al, Fe, Ca, Ti, and Mn), RSDs range from 2.1-4.0 %. Minor hydrothermal elements (V and As) range from 2.5-4.2 %. Other minor elements (Zn, Cr, Ni, Cu, and Mo) have a similar RSD range from 3.4-4.5 %. Aluminum concentrations fall just

under the published certified value for MESS-4 (2σ). Note that Al results were used to qualitatively cross-check Ti values but otherwise were not applied in our detrital correction method (see below). The remaining metal concentration values of MESS-4 fall within the published certified values.

Table 2: Average experimental values (± 2σ) of 12 element concentrations determined in the certified standard (MESS-4, *n* = 22).

Element	**MESS-4 certified value (±2σ)**	**MESS-4 (±2σ)**	**RSD**
Al (%)	7.91 ± 0.20	7.23 ± 0.47	2.1
Fe	3.79 ± 0.16	3.74 ± 0.27	3.2
Ca	1.31 ± 0.06	1.28 ± 0.09	3.5
Ti	0.38 ± 0.02	0.36 ± 0.03	4.0
Mn (ug/g)	298 ± 14	300 ± 20	3.1
V	216 ± 8	200 ± 13	2.5
Zn	147 ± 6	146 ± 12	3.4
Cr	94.3 ± 1.8	92.3 ± 4.6	3.6
Ni	42.8 ± 1.6	43.0 ± 3.6	4.1
Cu	32.9 ± 1.8	33.5 ± 2.8	4.2
As	21.7 ± 2.8	19.8 ± 1.8	4.2
Mo	2.53 ± 0.12	2.38 ± 0.10	4.5

Fe and Mn values were corrected for the influence of detrital basaltic debris using Ti concentrations and the Fe/Ti and Mn/Ti ratios of EPR basalts. Following Dunk and Mills (2006), we determined the detrital contributions by multiplying the Ti concentration of each sample by the Fe/Ti (8.1±0.3) and the Mn/Ti (0.1±0.01) of recent (0 to 0.12 kyr) EPR basalts (Schramm et al., 2005). The calculated detrital value was then subtracted from the total Fe or Mn concentration to determine the hydrothermal contribution. Detrital Mn corrections were approximately < 0.1 wt% and Fe corrections were < 0.5 wt% with the exception of core OC170-026-159, where the corrections approached 7 wt% in certain intervals (Figures 2, 3, 4).

d) Calcium Carbonate (%$CaCO_3$) Measurements

Percent calcium carbonate (%$CaCO_3$) was measured using coulometry at Lamont Doherty Earth Observatory. Each sample was introduced into an atmospheric CO_2-free system and acidified to release CO_2 contained in the $CaCO_3$. Analyses (n = 121) were made using a UIC CM5012 CO_2 Coulometer with a 44-sample automated carousel. A 5 µg subsample of the 500 mg homogenized bulk sediment sample was placed into each vial and diluted with 5mL of distilled water. The vials were then capped with sealed lids and placed into the carousel sequentially for processing. A pure $CaCO_3$ check standard was measured throughout the analysis to account for machine drift (n = 11, %$CaCO_3$ = 100.3 ± 0.6%).

Fluxes

Fluxes of hydrothermal components (Fe, Mn, and As) were determined using mass accumulation rates (MARs). The MARs and associated uncertainty are given in Tables 6 (Y71-07-53) and 7 (OC170-026-159) (see Appendix). The MARs were determined using the linear sedimentation rate (LSR) between age control points (in cm/kyr) and the sediment dry bulk density (DBD) (g/cm^3):

$$\mathrm{MAR} = \mathrm{LSR}\left(\frac{\mathrm{cm}}{\mathrm{kyr}}\right) * \mathrm{DBD}\left(\frac{\mathrm{g}}{\mathrm{cm}^3}\right) \quad (1)$$

$$\mathrm{LSR}\left(\frac{\mathrm{cm}}{\mathrm{kyr}}\right) = \frac{\text{Depth Difference}(\Delta z)}{\text{Age Difference }(\Delta t)} = \frac{z_2 - z_1}{t_2 - t_1} \quad (2)$$

The DBD was inferred using the empirical relationship between DBD and %$CaCO_3$ for eastern tropical Pacific sediments (Snoeckx and Rea, 1994). The empirical relationship between DBD and %$CaCO_3$ is based on 1110 core top sediment samples from 11°N to 5°S that are composed of primarily of $CaCO_3$, biogenic opal, and hemipelagic clay.

Although core Y71-07-53 does not fall within these two latitudes, core tops in the vicinity of Y71-07-53 have a similar composition to the eastern tropical Pacific sediments given the high carbonate content (69.8 ± 4.6 %, 1σ) and reasonably high opal concentrations (~30 %, measured on a carbonate-free basis (cfb)) (Dymond, 1981). Therefore, we use the equatorial Pacific relationship, assuming a DBD error of ± 0.03 g/cm^3 (Snoeckx and Rea, 1994). Core OC73-03-20 has a much lower average %$CaCO_3$ (~34 %) and very high metal concentrations compared to equatorial Pacific sediments. Because there are only two main sediments components for this core (carbonate and hydrothermal metals), the empirical relationship for estimating DBD isn't appropriate for this core. Additionally, the limited number of age control points makes it impractical to quantify MAR-based metal fluxes for core OC73-03-20.

Core OC170-026-159 has an average %$CaCO_3$ of ~63 % through most of its stratigraphy (MIS 1-5), but anomalously high detrital input during MIS 6 and Termination II. Unlike core OC73-03-20, it does have an adequate number of age control points, so we use an average DBD of 0.54 g/cm^3, which is the average DBD associated with 63 % $CaCO_3$. We assume a DBD error of ± 0.29 g/cm^3 to account for down core uncertainty in DBD, which is equivalent to a range in % $CaCO_3$ of 55 to 83 % (63 % ± 1σ). Note that MAR-based flux results from core OC170-026-159 should be treated as qualitative indicators for flux changes given the assumed DBD values.

Fe, Mn, and As accumulation rates were determined by multiplying the bulk sediment MAR by the fraction (μg X/g bulk sediment) of each metal (X):

$$\mathrm{MAR_X} = \mathrm{LSR}\left(\frac{\mathrm{cm}}{\mathrm{kyr}}\right) * \mathrm{DBD}\left(\frac{\mathrm{g}}{\mathrm{cm^3}}\right) * \mathrm{X_{fraction}} \qquad (3)$$

Uncertainty errors for metal fluxes are calculated assuming that error propagates for each variable in the MAR equation. Errors for age differences between control points are dependent

on the age uncertainty of ± ~3 kyr for $\delta^{18}O$ relative to the average difference between control points. This comparison influences the age difference error by ± 15%:

$$\Delta t_{error} = \pm 0.15 * \Delta t \quad (4)$$

The age control errors are propagated through the linear sedimentation rate errors:

$$LSR_{error} = \pm \left(LSR^2 * \frac{\Delta t_{error}^2}{\Delta t^2} \right)^{\frac{1}{2}} \quad (5)$$

Sedimentation rate errors and DBD errors, the standard error of estimate from the linear regression of the empirical relationship (Snoeckx and Rea, 1994), are then propagated through the MAR estimate:

$$MAR_{error} = \pm \left(MAR^2 * \left(\frac{DBD_{error}^2}{DBD^2} + \frac{LSR_{error}^2}{LSR^2} \right) \right)^{\frac{1}{2}} \quad (6)$$

Finally, errors for the metal MAR fluxes are generated using RSD (1σ) values of the MESS-4 standard for each element (X) (Table 2), the MAR error at each depth interval, and the MAR of each depth interval:

$$MAR_{X_{error}} = \pm \left(\left(\frac{X_{error}^2}{X_{fraction}^2} + \frac{MAR_{error}^2}{MAR^2} \right) * MAR_X^2 \right)^{\frac{1}{2}} \quad (7)$$

e) Pyroclastic Ash Size Fractions

The grain size distribution for basaltic glasses in the pyroclastic ash layer of OC170-026-159 was determined by isolating the ash shards using a series of acidification and washing steps. Sieves were stacked with mesh size in descending order: 500, 250, 125, 63, and 37 μm. Approximately 500 mg of sample was placed into the top sieve (500μm) and the stack gently shaken to distribute the sample. The sieves were gently rinsed in cold water until only basalt and

foraminifera were visible and each sieve was taken off as it was finished (not all clay was rinsed out at this step). The sieves were oven dried at 70°C until the samples were completely dry (< 1 hour). The samples were combined into one weighing dish and the forams dissolved with 2-3mL of 5% HNO_3. After the release of CO_2 subsided and foraminifera were no longer visible (about 5 minutes), the sieves were re-stacked in descending order and the acidified sample was gently rinsed into the top sieve. The samples were sieved again until clay was no longer visible and the sample appeared to be only basaltic debris. All sieves were dried again at 70°C and weighed individually by size fraction. Percentages of each fraction were calculated by dividing the difference between the initial and final mass by the final mass. Note that not all clay was rinsed out of the samples; excessive rinsing could have potentially broken the basalt shards and affected the size fraction distribution. Some of the remaining clay pieces were embedded with large pieces of basalt, and the weight they contributed to the sample is most likely negligible.

3. Results

a) Core Y71-07-53

Core Y71-07-53 was initially analyzed by Schaller et al. (2000) for Fe, Mn, V, As, Mo, and other metals. While their goal was to assess whether elements scavenged by hydrothermal iron oxides reflect seawater values, the bulk metal concentrations can also be used to assess input of hydrothermal plume particles to the core site. While Schaller et al. (2000) did not develop an age model for Y71-07-5, one of the goals of the recent study by Lund et al. (2016) and this study was to construct an age model for Y71-07-53 using $\delta^{18}O$ stratigraphy. The $\delta^{18}O$ stratigraphy for core Y71-07-53 outlines Marine Isotope Stages (MIS) 2-6, which span approximately 25-140 kyr BP (Figure 5a). During the MIS 6/5 transition (~130 kyr BP), also known as Termination II, $\delta^{18}O$ values increase from a positive, glacial value (~0.2 ‰) at 133 kyr BP to a more negative, interglacial value (~-1.3 ‰) by 118 kyr BP (Figure 5a). Percent $CaCO_3$ ranges from 50-80%, averaging 69.8 ± 4.6 % (1σ), which is within the expected range given the core's location along the northern edge of the subtropical gyre (Figure 12) (Dymond, 1981).

During MIS 6 (~160-140 kyr BP), hydrothermal Fe and Mn concentrations were low, measuring in at ~4.7 wt% and 1 wt%, respectively (Figure 5b). Following MIS 6, Fe and Mn increase markedly and peak at the end of Termination II (~ 135-125 kyr BP). The maximum concentrations persist into MIS 5e (~117 kyr BP), with Fe values of ~11 wt% and Mn values of ~ 2.4 wt%. In both case, the peaks' values are 2x larger than background MIS 6 concentrations. As concentrations increase ~5x from 44 μg/g during MIS 6 to ~230 μg/g during TII, while V concentrations increase ~3x from 95 μg/g to 280 μg/g (Figure 5c). Titanium concentrations are low throughout the core (<280 μg/g) and suggest there is little input of detrital material to the

core site (Figure 5d). Similar to Ti, aluminum concentrations are low throughout the core (<2000 μg/g) (Figure 5d). Given the low Ti and Al values, detrital corrections for core Y71-07-53 were minimal (Figure 2).

The metal concentration data for core Y71-07-53 combines data from Schaller et al. (2000) and this study. During TII, select Fe points from Schaller et al. (2000) appear to be anomalously high relative to our results. To assess the discrepancy, we requested photographs and sample log records of the working and archive halves of core Y71-07-53 (Figure 13). In each study, sediments were preferentially sampled from the working half of the core, followed by sampling from the archive half if there was insufficient working half material to sample. After a careful inspection of the core photos, we determined that there is no clear offset between our results and those of Schaller et al. (2000) due to sampling depth errors. Rather, the mottled appearance of the core suggests that bioturbation created centimeter-scale heterogeneity in the core samples. We suggest that sampling bias could play a role in the systematically higher results from Schaller et al. (2000). For example, Schaller et al. (2000) report five, one cm-thick samples from 150-200 cm, while this study reports eight, two cm-thick samples from the same interval. Additionally, 200 mg of sediment used in the metal analyses from this study is subsampled from 500 mg of ground, homogenized sample for each depth interval. The larger sample size and more frequent sampling reported in this study help to homogenize variability in the core caused by bioturbation. Because Schaller et al. (2000) used smaller samples and sampled less frequently, it is likely that their results are more susceptible to core heterogeneity.

b) Core OC73-03-20

The results for core OC73-03-20 at 19°S span from approximately 40 kyr BP to the present. The $\delta^{18}O$ stratigraphy outlines MIS 1-3, which includes Termination I (18 kyr BP to 8 kyr BP) (Figure 6a). From 23 kyr BP to 20 kyr BP, the average $\delta^{18}O$ was ~-0.3 ‰, indicating the approximate LGM time interval (23-19 kyr BP). From 20 kyr BP to 15 kyr BP, $\delta^{18}O$ rapidly increased from -0.3 ‰ to -1 ‰, and then increased more gradually from -1 ‰ to -1.2 ‰ from 15 kyr BP to 6 kyr BP, representing the transition from glacial to interglacial conditions. The $\%CaCO_3$ for this site ranges from 8 % to 46 %, with an average value of 34.2 ± 12.9% (1σ), the lowest of the three locations (Figure 6a). Carbonate values are exceptionally low (~10%) during TI, most likely due to the very high metal concentrations in this interval (Figure 6a,b).

Iron and manganese concentrations roughly double from ~11.5 wt% Fe and ~4 wt% Mn during the LGM (23-19 kyr BP) to ~25 wt% Fe and ~7.5 wt% Mn by the middle of TI (Figure 6b). The maximum concentrations of Fe and Mn slightly precede TI but age model error (± 3 kyr) precludes a clear determination of the relative timing. Peak concentrations in As and V occur during the same timeframe as Fe and Mn, where As increases from ~210 μg/g (LGM) to ~500 μg/g (TI) and V increases from ~350 μg/g (LGM) to ~800 μg/g (TI) (Figure 6c). Titanium and aluminum concentrations range from 80 to 870 μg/g and from 650 to 4700 μg/g, respectively (Figure 6d). Detrital corrections are therefore minimal for core OC73-03-20 (Figure 3).

c) Core OC170-026-159

Core OC170-026-159, located at 39°S, spans both TI and TII. The $\delta^{18}O$ results clearly outline MIS 1-6 (Figure 7a). From 140 kyr BP to 125 kyr BP, $\delta^{18}O$ values rapidly decrease from

1.5 ‰ to 0 ‰, reflecting the transition from MIS 6 to MIS 5e (i.e. TII). The MIS 5/4 transition occurs at ~72 kyr BP (~0.9 ‰), followed by the MIS 4/3 transition at ~57 kyr BP (~0.86 ‰), and finally the MIS 3/2 transition at ~30 kyr BP (~1.25 ‰). The MIS 2/1 transition (~15 kyr BP) is represented by the change in $\delta^{18}O$ from 1.4 ‰ (~20 kyr BP) to 0.2 ‰ (8 kyr BP). The $\%CaCO_3$ values for core OC170-026-159 range from 34-76%, with an average value of 62.9 ± 13.7% (1σ) (Figure 7a). Percent $CaCO_3$ during MIS 6 and TII is exceptionally low (34.6%) because the bulk of the sediment during this time is dominated by volcanic glass (Figure 7a,d).

Core OC170-026-159 shows hydrothermal patterns consistent with the other sample sites in this study. Iron and manganese percentages begin to increase during TI and TII, suggesting greater deposition of hydrothermal particles (Figure 7b). During MIS 6, Fe and Mn concentrations are at minimum values of ~2.2 wt% and 0.7 wt%, respectively. These concentrations are unusually low due largely to the 10-fold increase in basaltic debris from 148 to 130 kyr BP (Figure 7d). During the MIS 6/5 transition, Fe and Mn increase to a maximum of 7.5 wt% (Fe) and 3 wt% (Mn) by the end of TII and into MIS 5e (~120 kyr BP). A similar phenomenon occurs from the LGM to TI, with baseline values starting at 5.3 wt% (Fe) and 1.9 wt% (Mn) during the LGM and increasing to concentrations of 7.3 wt% (Fe) and 3.2 wt% (Mn) during the middle of TI (Figure 7b). Comparable to the other cores, peak concentrations in As (108 μg/g) and V (230 μg/g) coincide with peak Fe and Mn concentrations during TI, suggesting that the As and V were scavenged from seawater by Fe oxyhydroxides and Mn oxides (Figure 7c). During TII, however, the peak V concentration (260 μg/g, 137 kyr BP) precedes the As peak (100 μg/g, 124 kyr BP) by about 13 kyr.

Core OC170-026-159 is unusual in that there are prominent peaks in Ti and Al that align with TII (Figure 7d). At TII, the Ti and Al levels increase ten-fold to 7500 μg/g (Ti) and $4*10^4$ μg/g (Al), far higher than any Ti or Al concentrations in any of the cores presented here or in earlier studies (Schaller et al., 2000; Lund et al., 2016). By comparison, Ti concentrations ranged from 200-800 μg/g and Al concentrations ranged from 2000 to 5000 μg/g during TI, similar to the results for the other cores presented here. Detrital corrections for Fe and Mn in OC170-026-159 during TII are the highest of all study sites, reaching almost 7 wt% Fe during the peak Ti concentration (Figure 4, see Methods).

Upon inspection of the bulk sediment, we found microscopic pyroclastic ash debris in the depths of the titanium peak (Figure 11). The morphology of the basalt pieces are both fluidal and shard-like, with limu o Pele forms ranging from bubble-wall fragments (Figure 11b), to rods (simple, twisted, or bent) (Figure 11c,d), and ribbons (flat, twisted, bent, or folded) (Figure 11e,f,g) (Clague, Paduan, and Davis, 2009).

d) Combined MAR-based Flux Data

MAR-based metal fluxes of Fe, Mn, and As for core Y71-07-53 are shown in Figure 8. Linear sedimentation rates range from 0.8 to 2.5 cm/kyr throughout the core. From MIS 6 to MIS 5e, flux values for Fe roughly double from 60 to 130 μg cm^{-2} yr^{-1} (Figure 8b). Maximum fluxes persist into MIS 5e (~120 kyr BP). Similar patterns are reported for Mn and As fluxes Figure 8c, d). While core Y71-07-53 does not actually capture the MIS 2/1 transition, there are sediment cores from nearby locations do (Lund et al., 2016). Cores Y71-07-49 and Y71-07-51 at 11°S from Lund et al. (2016) also show an approximate doubling of fluxes during TI, with Fe

values increasing from ~22 to ~40 μg cm^{-2} yr^{-1}. Manganese and arsenic fluxes show similar patterns.

MAR-based metal fluxes for core OC170-026-159 are tentative given the assumed constant DBD, but still provide qualitative trends in hydrothermal activity. Linear sedimentation rates range from 0.10 to 1.3 cm/kyr throughout the core. Flux estimates from this core record a similar pattern to core Y71-07-53 in that there is a marked increase in Fe, Mn, and As fluxes from baseline values during glacial periods to maximum values during glacial terminations. This occurs for both TI and TII in core OC170-026-159. From the LGM to TI, the linear sedimentation rate shifts from 0.97 to 1.30 cm/kyr. The exact shift occurs at ~22 kyr BP, mainly due to the age control point chosen for the age model. Fe fluxes roughly double from 30 μg cm^{-2} yr^{-1} during the LGM to 55 μg cm^{-2} yr^{-1} during TI (Figure 9b). Manganese and arsenic values follow similar patterns (Figure 9c,d).

Sedimentation rates increase from 0.76 to 1.10 cm/kyr during the later portion of MIS 6 (~153-140 kyr BP) to TII at ~130 kyr BP, which is a similar shift in sedimentation rates relative to the LGM to TI transition (~0.3 cm/kyr). While the Fe fluxes begin to increase simultaneously with the shift in sedimentation rate during TI, increasing flux values slightly precede the sedimentation rate shift during TII (~133 to ~130 kyr BP). Regardless, the maximum rate of change in the Fe flux occurs at the shift in sedimentation rate (~130 kyr BP). From the sedimentation rate shift alone, we expect a ~2x increase in fluxes. However, unlike the first deglaciation, our estimates suggest there is a ~5-6x increase in fluxes from MIS 6 to the MIS 5e (Figure 9). From MIS 6 to the end of TII, Fe flux increases from ~8 μg cm^{-2} yr^{-1} to ~45 μg cm^{-2} yr^{-1} (Figure 9b). Mn and As fluxes behave similarly to Fe fluxes (Figure 9c,d). Based on the

~4x increase in Fe concentrations during this transition (~2 % to 8 %), a larger flux increase is reasonable. However, the flux estimate does not take into account that the $\%CaCO_3$ falls below 1σ for the DBD approximation during this time interval, which may overestimate the flux results. Additionally, the ~10x increase in Ti and Al concentrations from the pyroclastic ash layer (~148-130 kyr BP) is not accounted for in the DBD estimate. Without better constraints on the DBD estimate, the magnitude of the flux estimates that fall during the TII ash layer should not be considered as quantitatively accurate.

Overall, the flux data for cores Y71-07-53 and OC170-026-159 is consistent with the metal concentration data for both Terminations I and II. Metal concentrations for core Y71-07-53 at 11°S roughly double during TII, which is reflected as an approximate doubling of the MAR-based metal fluxes during the same time period. Additionally, flux estimates from nearby sites at 6°S and 11°S from Lund et al. (2016) reflect similar doubling patterns of metal fluxes during TI. Metal concentrations from core OC73-03-20 (19°S) roughly double as well during TI. However, MAR-based metal flux estimates were not calculated based on the limited number of age control points. Metal concentrations and metal fluxes for core OC170-026-159 (39°S) roughly double between the LGM and TI. The concentration and flux values both show an increase from MIS 6 to TII, but the magnitudes of the changes are less tightly correlated. The metal concentration data increase by ~4x, while the MAR-based flux data increase by ~5-6x during MIS 6 to TII. It is likely that the lower $\%CaCO_3$ and pyroclastic ash layer skews the DBD estimate during this time period, overestimating the final flux approximations.

4. Discussion

At three sites along approximately 2000 km of the southern East Pacific Rise and Pacific Antarctic Ridge, we observe evidence consistent with enhanced hydrothermal activity during the last two glacial terminations. Maximum Fe and Mn concentrations peak during TI in cores OC73-03-20 and OC170-026-159 and TII in cores Y71-07-53 and OC170-026-159. The overall pattern is similar to that observed in locations along the SEPR at 6°S and 11°S (Lund et al., 2016) and the East Pacific Rise (EPR)–Dietz volcanic-ridge triple junction (1°N) (Frank et al., 1994; Lund et al., 2016). The trends in Fe and Mn are supported by similar down core concentration patterns in As and V, which are scavenged from seawater during the precipitation of hydrothermal Fe oxyhydroxides and Mn oxides (Dymond, 1981; Morford and Emerson, 1999; Schaller et al., 2000; Cave et al., 2002).

There are several possible explanations for the patterns in metal concentration along the EPR and PAR, the most likely of which is regional scale changes in hydrothermal activity. Several confounding factors deserve consideration, however, including diagenetic remobilization, dilution by non-hydrothermal components, and horizontal sediment focusing. These factors are discussed in detail below. Although the possibility of diagenetic remobilization cannot be completely discounted, such an explanation is highly unlikely given the available data. The pyroclastic ash shard layer in core OC170-026-159 will also be discussed and linked to explosive submarine volcanism activity along the PAR. Finally, potential implications of the results for climate variability will be outlined as areas for future research.

a) Potential confounding factors

i) Diagenetic Remobilization

Diagenetic remobilization of metals in marine sediments is driven by the relative availability of reductants (electron donors) and oxidants (electron acceptors). While organic matter acts as the primary electron donor, there are multiple potential electron acceptors, including O_2, MnO_2, and FeOOH, amongst others. Oxidation of organic material follows a predictable hierarchy of oxidants, with the order based on the free energy change per mole of carbon oxidized (Froelich et al., 1979; Emerson and Hedges, 2004). Once the electron acceptor with the greatest energy change is depleted, the next most efficient oxidant will be used. In marine sediments, the hierarchy of oxidants is as follows:

$$O_2 > MnO_2 \sim NO_3^- > FeOOH > SO_4^{2-} \quad (8)$$

Oxygen is the first oxidant to be exhausted, followed by MnO_2 and NO_3^-, then FeOOH, and eventually SO_4^{2-}. If there are insufficient quantities of one electron acceptor, a less efficient but more abundant oxidant will be used instead. The oxidation of organic carbon depends on the environment in which it is found. For example, O_2 acts as the main electron acceptor in oxic environments; MnO_2, NO_3^-, and FeOOH reduction occurs in suboxic environments; and SO_4^{2-} is reduced in anoxic environments (Froelich et al., 1979). A schematic diagram of the sequence of redox processes is shown in Figure 14. The main activity in Zone 1 is the reduction of O_2 in the pore waters by organic matter. Oxidized organic matter forms NH_4^+, which is then oxidized further by nitrobacteria to form NO_3^-, which is neither consumed nor produced in Zone 2 (Froelich et al., 1979).

Manganese oxide reduction begins when the consumption rate of oxygen via oxic diagenesis exceeds the rate of oxygen diffusion from the seawater-sediment interface. Reduction of MnO_2 creates free Mn^{2+} in pore waters, creating a gradient of high Mn^{2+} concentrations below the zone of oxic diagenesis to a near zero levels as it approaches the oxic zone (Figure 14, Zone 4). The Mn^{2+} migrates vertically through the profile until it encounters O_2 and is oxidized, forming solid phase MnO_2 in discrete layers. Because manganese-rich layers are precipitated from pore waters, they may not necessarily be formed at the same time as sediments at the same stratigraphic level. This phenomenon, known as a manganese trap, occurs in the sediment column from the balance of O_2 diffusing downward and Mn^{2+} diffusing upward. A MnO_2 spike in the depth profile represents this process (Figure 14, Zone 3) (Froelich et al., 1979). Depending on the redox conditions at a given location, the MnO_2 layer may occur very close to the seawater sediment interface or much deeper in the sediments if organic carbon concentrations are low and there is little O_2 demand from decomposition of organic matter (Lyle, 1983).

The reduction and remobilization of Fe(III) to Fe(II) proceeds in a similar manner to that of Mn, except that it occurs deeper in the pore water profile. After Fe(III) (FeOOH) is reduced by organic matter, Fe(II) is released into Zone 7 (Figure 14). At the approximate depth where NO_3^- concentrations approach zero (Zone 5), Fe(II) cations travel upward through the pore water and are oxidized to form FeOOH at the top Zone 6 (Lyle, 1983).

It is unlikely that sediment diagenesis is altering Fe and Mn concentrations at the SEPR and PAR core locations for four key reasons: 1) the background redox conditions vary with latitude based on primary productivity and organic carbon concentrations in the sediments, 2) concentrations of organic carbon are too low to remobilize Fe, 3) contemporaneous Fe and Mn

peaks occur in each sediment core, while the hierarchy of oxidants implies that Fe and Mn should be offset in depth, and 4) the down core Fe/Mn ratio in the sediments is similar to that expected for hydrothermal particles.

1) Background Redox Conditions

In order for diagenetic remobilization to cause coherent peaks in hydrothermal metal concentrations along 4500 km of mid-ocean ridge, the background redox conditions must be consistent. Based on the north-south gradient in primary productivity, export productivity, and the redox boundary depth conditions observed at different core locations, however, it is unlikely that redox conditions are the same at each core site. The concentration of organic carbon (C_{org}) can be used to assess the overall oxygen demand in marine sediments. Core sites at 1°N and to a lesser extent 5-6°S fall within the highly productive equatorial Pacific; as a result, C_{org} concentrations range from 0.4-0.6 wt% at 1°N to 0.2-0.4 wt% at 5-6°S (Lyle, 1992). At 11°S, which is the northern edge of the oligotrophic subtropical gyre, C_{org} concentrations are generally less than 0.2 wt% (Schaller et al., 2000; Mills et al., 2010). Further south, C_{org} continues to decrease, reaching values of < 0.06 wt % in the center of the subtropical gyre at 20°S (Marchig and Gundlach, 1982; Shimmield and Price, 1988).

Concentrations of biogenic opal in eastern Pacific sediments mirror the trend in organic carbon at these sites, with > 70% biogenic opal at 1°N and dropping to < 10% by 39°S (Dymond, 1981). (The biogenic opal values are reported on a carbonate and salt-free basis.) The north-south trends in organic carbon and biogenic opal are supported by the gradient of surface water phosphate concentrations, which can be used as a qualitative indicator of export production from

the photic zone (Figure 12). At 11°S, phosphate concentrations are approximately 0.6 μmol/L, while at 19°S phosphate levels approach zero (< 0.01 μmol/L) before rebounding to 0.4 μmol/L at 39°S (Figure 12). Coherent patterns in Fe and Mn peaks during glacial terminations would suggest that overall oxygen demand was similar at sites from 0° to 40°S. Based on the north-south gradient in C_{org}, biogenic opal, and phosphate concentrations, it is highly unlikely that background redox conditions were similar at all three core sites.

Organic carbon export to the seafloor may also be assessed by the sedimentary depth of the Fe(III)-Fe(II) redox boundary. Higher organic carbon fluxes to the seafloor create a higher oxygen demand and therefore increase the likelihood of MnO_2 and FeOOH reduction. Lyle (1983) noted that hemipelagic sediments have an observed brown "oxidized" layer above a green "reduced" layer of sediment. Brown sediments are mainly composed of oxidized iron (Fe(III)) and the green layer is the reduced form (Fe(II)). These observations were verified with porewater NO_3^- and Fe concentrations (Lyle, 1983), which show that the boundary layer depth increases with increasing distance from the continents. The Fe(III)-Fe(II) boundary layer lies within 2 cm of the surface sediments near the coastline, steadily increasing until it lies well below 100 cm at the ridge crest. Thus, the thickness of the surface brown layer can be used to qualitatively assess the depth at which iron species begin to transition from the oxidized to the reduced forms.

If diagenetic remobilization of iron drove coherent metal concentration peaks, we would predict that the Fe(III)-Fe(II) redox boundary layer would be in the upper 20-30 cm of sediments during the deglaciation at each sample location. At 1°N and 6°S, however, the modern boundary occurs between depths of 50 to 100 cm (Lyle, 1983). At 11°S and 19°S, the Fe(III)-

Fe(II) redox boundary occurs at depths greater than 100 cm. The sample logs for Y71-07-53 and OC73-03-20 do not include observations of any brown to green color transition at any depth, let alone the upper 20-30 cm of each core. Core Y71-07-53 is approximately 5 m in length, so the Fe(III)-Fe(II) transition must occur at a greater depth. Core OC73-03-20 is approximately 2 m in length, implying that the Fe(III)-Fe(II) transition occurs at >2 m depth in the sediment column. In order for the remobilization of Fe(III) to Fe(II) to concurrently occur at all sites during the deglaciation, the boundary would have had to migrate from ~20 cm to more than 2 m today, suggesting a radical change in redox conditions. Such an extreme shift suggests the oxidation of Fe(II) to Fe(III) an unlikely driver of the ridge-wide patterns of increased Fe during Termination I.

2) Low Organic Carbon Concentrations

Low organic carbon concentrations at 11°S and 19°S are the second key factor that indicates diagenetic remobilization is an unlikely driver of the Fe signals. Put simply, the concentrations of C_{org} are too low to mobilize the observed quantities of Fe. One mole of organic carbon is required to reduce four moles of FeOOH (Froelich et al., 1979; Emerson and Hedges, 2004). The relevant redox reaction is:

$$(\mathbf{CH_2O})_{\mathbf{106}}(NH_3)_{16}(H_3PO_4) + \mathbf{424FeOOH} + 848H^+ \rightarrow$$
$$424Fe^{2+} + 106CO_2 + 16HNO_3 + H_3PO_4 + 742H_2O \qquad (9)$$

In addition to the required 1:4 moles of C_{org} to FeOOH, the atomic weight of Fe is ~4.5 times that of C. Therefore, an original organic carbon concentration of approximately 0.5% would be required to mobilize and create an Fe peak of 10 % (by weight).

Core Y71-07-53 is on the northern edge of the subtropical gyre, meaning that overall organic carbon export to the sediments is low. In order to create the ~11 wt % Fe maximum at TII, it would have required ~0.6 wt% of C_{org} in the sediments. Given that the measured organic carbon values at this site average 0.1 – 0.2 wt % (Schaller et al., 2000), the original concentration of C_{org} would have exceeded 0.7 wt %. Given that this estimate is >3x the observed C_{org} values in core Y71-07-53, it unlikely that suboxic diagenesis created the Fe peak at 11°S.

Similarly, it is unlikely that the Fe peak in core OC73-03-20 (19°S) during T1 was driven by diagenetic remobilization because of the very small amount of organic carbon present in nearby sediments (0.06% - (Marchig and Gundlach, 1982; Shimmield and Price, 1988). In order to remobilize 25 wt% Fe during TI, it would require an average C_{org} concentration of ~1.3 wt%. This estimate is ~20x higher than the observed values in the vicinity of core OC73-03-20 (Marchig and Gundlach, 1982; Shimmield and Price, 1988). Thus, the sheer quantity of Fe and the overall lack of C_{org} suggest that Fe peak during Termination I was not a byproduct of diagenetic remobilization.

3) Contemporaneous Fe and Mn peaks

The redox potentials of Fe oxyhydroxides and Mn oxides are significantly different, providing a third reason that diagenetic remobilization of Fe and Mn is unlikely to cause coherent metal concentration peaks. A redox reaction is more likely to spontaneously occur if the calculated Gibbs free energy has a large, negative magnitude. Organic matter reduction of oxygen has the largest negative change in Gibbs free energy (-3200 kJ/mol), which means that it is energetically favorable to use oxygen first. The reduction of Mn oxides to Mn(II) by organic

matter is the next most spontaneous reaction as it has a free energy of -3000 kJ/mol, while FeOOH reduction has a much lower free energy of -1300 kJ/mol. Note that the Gibbs free energy changes of O_2, FeOOH, and MnO_2 were calculated at STP and at a biochemical reference state (pH 7) (Froelich et al., 1979). Based on distinctly different redox potentials and assuming constant C_{org} concentrations, we would predict that Mn(II) would move through the sediment column independently of Fe and precipitate out at a different depth. Thus, if sediment diagenesis was the primary driver of the metal signals along the EPR, we would expect Mn and Fe maxima to occur at different depths within the sediment cores.

If diagenetic remobilization was the main driver of these metal peaks, it would require that bottom water oxygen concentrations and exported organic material concentrations be specifically tailored to each region over at least two glacial terminations. Cores at 1°N from Lund et al. (2016) and 19°S from this study show the most contrasting organic carbon results given each core's location relative to the subtropical gyre. Without suboxic bottom water oxygen concentrations, neither site would promote Fe or Mn diagenesis. Manganese concentrations provided by Frank et al. (1994) and Lund et al. (2016) at 1°N indicate that MnO_2 from down core (>20 kyr BP) underwent diagenesis and was remobilized to the location of the Fe maxima. Given the relatively higher organic carbon concentrations in the highly productive equatorial Pacific (0.4-0.6 wt% - Lyle, 1992), it is possible for small amounts of Fe remobilization to occur. If this same phenomenon were to occur at 19°S, where the organic carbon values are two orders of magnitude lower than at 1°N, Fe remobilization would require a tripling of the export of organic matter to the seafloor at this specific location. This is unrealistic

given that the core underlies the subtropical gyre, where increases in organic carbon export are minimal to begin with.

At each site, we see contemporaneous Fe and Mn peaks within the limits of the age model. While diagenetic remobilization likely plays a role in modifying Mn records at sites close to the equator (Lund et al., 2016) the overall similar pattern in Fe, Mn, and As records from 1°N to 40°S suggests that hydrothermal activity acts as the first order control on down core metal concentrations.

4) Fe/Mn ratios consistent with hydrothermal end member

The final reason that it is unlikely that sediment diagenesis played a primary role in setting Fe and Mn concentrations at 11°S, 19°S and 39°S is that each has Fe/Mn ratios consistent with hydrothermal input. A study of the Nazca Plate surface sediments compared Fe and Mn concentrations (wt %) for core tops within 100 km of the East Pacific Rise (Dymond, 1981). A normative sediment analysis model was used to separate the bulk sediment into five sources based on elemental ratio coefficients, including Fe/Mn. The hydrothermal source term was characterized by a relatively constant Fe/Mn weight percentage ratio of 3.5 ± 0.9 (1σ). This ratio was determined by averaging the core top data within 100 km of the EPR and measuring the standard deviation. The source term was confirmed by examination of elemental ratios of metal rich samples collected close to the ridge crest (Dymond, 1981). Multiple studies have confirmed similar Fe/Mn values in EPR sediments (Metz, Trefry, and Nelsen, 1988; Shimmield and Price, 1988; Frank et al., 1994; Schaller et al., 2000; Dunk and Mills, 2006; Mills et al., 2010; Lund et al., 2016).

Fe/Mn ratios for all depth intervals in each core are shown in Figure 15. The Fe/Mn ratios at 11°S range from 2.9 to 7.8, with an average of 4.8 ± 0.85 (1σ). Although the average ratio falls within 2σ of the calculated value, this location has the highest Fe/Mn ratio of the three, implying that Mn remobilization may have occurred at this site. However, rhenium concentrations measured in this core, which are authigenically enriched in reducing sediments, were reported at detrital levels, suggesting that reducing conditions were not suitable to remobilize Fe (Morford and Emerson, 1999; Schaller et al., 2000). Furthermore, given the low C_{org} levels at 11°S, it is unlikely that remobilization created the Fe concentration peak.

Fe/Mn ratios at 19°S are lower than 11°S, averaging 3.5 ± 0.34 (1σ), indistinguishable from the hydrothermal endmember value. The Fe/Mn values suggest there was little to no diagenetic impact on MnO_2 at 19°S, consistent with the low sedimentary biogenic opal and organic carbon concentrations in this region. The Fe/Mn ratio at 19°S is nearly constant from from 20 to 5 kyr BP, with an average of ~3.2. Prior to 21 kyr BP, slightly higher Fe/Mn ratios occurred, averaging Fe/Mn ~3.4. The consistent Fe/Mn values at 19°S imply that hydrothermal activity was the primer driver of coherent Fe and Mn peaks during TI.

Finally, Fe/Mn ratios at 39°S average 2.9 ± 0.65 (1σ), which is lower than the average hydrothermal end member and the other two sites. The average down core Fe/Mn ratio for core OC170-026-159 is close to the only measured core top from this region, with an Fe/Mn ratio of 2.4 (Dymond, 1981). Core OC170-026-159 is located on the PAR, which has a lower half-spreading rate (~49 mm/year) compared to the SEPR (~75 mm/year) (Figure 1). A lower half-spreading rate could decrease the temperature at which hydrothermal fluids interact with vent systems, potentially altering the Fe/Mn ratio of hydrothermal fluids (Haymon, Kastner, and

Kerridge, 1979; Hekinian et al., 1980). The lack of a well-defined hydrothermal end member for the PAR precludes us from determining whether diagenetic remobilization of Mn is occurring at 39°S. Based on the location of the core relative to the edge of subtropical gyre and the minimal qualitative export of biogenic material to the seafloor (Figure 12), however, it is unlikely that there is enough C_{org} to remobilize Fe oxyhydroxides.

Based on the arguments outlined above, it is unlikely that diagenesis is an important driver of Fe and Mn maxima at glacial terminations at the SEPR and PAR. There are varied background redox conditions at the three different latitudes as indicated by changes in organic carbon, biogenic opal concentrations, and the depth of the Fe(III)-Fe(II) redox boundary. Although there may be some suboxic Mn diagenesis occurring in core Y71-07-53, low organic carbon levels at all three sites inhibit the remobilization of Fe. The contemporaneous Fe and Mn peaks occur in each sediment core spanning Terminations I and II, regardless of the hierarchy of oxidants in the pore water profiles. Finally, the down core Fe/Mn ratio in the sediments is within 2σ of core top Fe/Mn ratios measured by Dymond (1981). Taken as a whole, hydrothermal input, as opposed to diagenesis, appears to be the primary driver of the Fe and Mn signal found at the SEPR and PAR.

ii) Dilution by Non-hydrothermal Components and Horizontal Sediment Focusing

The metal concentration data for the three cores suggests that enhanced hydrothermal activity occurred during the last two glacial terminations. However, hydrothermal metal concentrations are subject to dilution by other sedimentary components, including $CaCO_3$, biogenic opal, and detrital input of basaltic debris. Core OC73-03-20 is predominantly

composed of hydrothermal metals and $CaCO_3$, creating an inverse relationship between metal and $CaCO_3$ concentrations. Weight percentages alone cannot distinguish between increased metal input or decreased $CaCO_3$ input during Termination I. The composition of core OC170-026-159 has a similar problem due to the ~10x increase in Ti and Al concentrations during TII. The weight percentage of hydrothermal Fe drops from 7 wt% at ~190 kyr BP to 1.3 wt% at 140 kyr BP, most likely due to the dilution from basaltic debris.

We can address potential dilution of the hydrothermal signal by calculating metal fluxes using sediment mass accumulation rates (MARs). MARs reflect the bulk accumulation rate of sediment and are determined using the sedimentation rate between age control points (cm/kyr) and the dry bulk density (DBD in g/cm^3) of the sediments (see Methods). Metal fluxes are simply determined by multiplying the percent of given component (e.g. Fe) by the MAR. Thus, the dilution effect is in theory accounted for by MARs because any large changes in non-hydrothermal components (e.g. $CaCO_3$) will be reflected in the MAR itself. If sedimentation rates and DBD for a given core are relatively constant through time, then the MARs will be as well, and the metal fluxes will have similar down core patterns to the companion weight percent record.

Although MARs are widely used because of their convenience and simplicity (including in this study), there are several major shortcomings of this approach. First, mass accumulation rates have a characteristically low temporal resolution that is set by the distance between age control points (Francois et al., 2004). To increase the temporal resolution, additional age control points are necessary, but this then increases the relative age error for each time interval. Age control points based on oxygen isotope stratigraphy have a ± 3-4 kyr error, which can drastically

affect the sedimentation rates and therefore the MAR estimates. Second, MAR estimates depend on dry bulk densities of the sediment, which can be estimated by determining the mass difference between wet and dry sediments or by creating linear or polynomial fits with measured carbonate concentrations (Snoeckx and Rea, 1994; Francois et al., 2004). Measuring preserved, wet sediments was not an option for this study as the core samples have been in storage for over 40 years. Additionally, the three cores were sampled in locations with different regional sediment lithologies, which would require extensive sampling of each region to establish region-specific, empirical DBD-$CaCO_3$ relationships. Finally, MAR estimates cannot distinguish sediment fallout from the water column from horizontal sediment fluxes driven by changes in bottom water currents. It is possible that horizontal sediment focusing or winnowing could alter MARs and give the false impression that the flux variations were due to variable input from the overlying water column.

In order to account for the shortcomings of the mass accumulation rate method, extraterrestrial ^{3}He isotopes can instead be used to constrain the bulk sediment flux. The premise of the method is that ^{3}He flux remains constant on Milankovitch timescales and if one knows the ^{3}He concentration of the sediments, it is possible to determine how much ^{3}He signal has been diluted by the bulk sediment flux. The extraterrestrial ^{3}He flux ([1.0±0.2] x 10^{-15} cm^3 STP cm^{-2} yr^{-1}) (Marcantonio et al., 1998) is divided by the concentration of ^{3}He at any given depth (in cm^3 STP g^{-1}) (Farley, Montanari, and Coccioni, 2012) to determine the sediment flux (in μg cm^{-2} yr^{-1}) at that stratigraphic level. The ^{3}He method is optimal for measuring fluxes because unlike the MAR method, it does not rely on age control points. Instead, it allows for estimates of sediment flux at the depth of each metal analysis, dramatically improving the resolution of the resulting

metal flux time series. Horizontal sediment focusing and winnowing can be accounted for by dividing the measured and predicted ^{3}He inventory for distinct depth intervals within each core. Ratios that are greater than 1 indicate sediment focusing, while ratios less than 1 indicate sediment winnowing (Lund et al., 2016).

While the analysis of ^{3}He isotopes is beyond the scope of this thesis, ^{3}He-based flux results from nearby cores along the EPR (Lund et al., 2016) can be used to assess the overall reliability of our MAR-based fluxes at 11°S. Iron and manganese fluxes estimated using the ^{3}He technique for core Y71-07-49 at 11°S show roughly a doubling from the LGM to TI. The flux of Fe increased from ~21 to ~41 μg cm^{-2} yr^{-1} and Mn increased from ~6 to ~13 μg cm^{-2} yr^{-1}. Fluxes for core Y71-09-106 at 6°S also display a similar pattern, with metal fluxes roughly doubling from the LGM to TI. Fe flux values increase from ~12 to ~32 μg cm^{-2} yr^{-1} and Mn values increase from ~2 to ~8 μg cm^{-2} yr^{-1}. The overall trend in the ^{3}He-based results is broadly consistent with MAR-based results for this core (Lund et al., 2016) and the results presented here (Figures 8b, c). During the MIS 6/5 transition, MAR-based Fe fluxes in core Y71-07-53 increased from ~60 to ~130 μg cm^{-2} yr^{-1} while Mn fluxes increase from ~10 to ~27 μg cm^{-2} yr^{-1}. An approximate doubling of MAR-based Fe and Mn fluxes also occurs in OC170-026-159 during TI. Iron increases from ~30 to ~55 Fe μg cm^{-2} yr^{-1} and Mn increases from 10 to 25 μg cm^{-2} yr^{-1} (Figure 9b,c). Helium isotope analyses for cores OC73-03-20 and OC170-026-159 will help clarify whether the concentrations accurately reflect changes in metal flux to the sediments.

b) Coherent Timing of Metal Concentrations

The coherent timing between maximum hydrothermal metal concentrations and glacial terminations suggests that there may be a relationship between changes in sea level and hydrothermal activity. The physical mechanisms of decompression melting, melt migration to the ridge axis, and expressions in proxies of hydrothermal activity represents a complex set of geophysical and geochemical processes. Melt must migrate from the magma source to the ridge axis, which likely takes thousands of years due to the slow melt extraction velocities in the upper mantle, ranging from >1 m/yr to 50 m/yr (Kelemen et al., 1997; Maclennan et al., 2002). Therefore, proxies of magmatic activity should lag sea level by 1 to 50 kyr (Lund and Asimow, 2011).

During the LGM, the largest drop in sea level occurred from 30 to 25 kyr BP (Clark et al., 2009), which is approximately 14 ± 4 kyr before the inferred maximum in SEPR hydrothermal activity for core OC73-03-20 during Termination I. Similarly, the LGM drop in sea level precedes the inferred maximum in PAR hydrothermal activity by 15 ± 2 kyr in core OC170-026-159. A lagged response also appears to occur following the rise in sea level from 18 kyr BP to 8 kyr BP. Rising sea level should dampen melt production and result in diminished hydrothermal activity. The results from OC73-03-20 and OC170-026-159 indicate a late Holocene minimum in hydrothermal metal concentrations for both cores (Figures 6, 7). Given the uncertainty in core top age for these cores, it is difficult to determine the exact time lag, but it appears to be on the order of 10-15 kyr BP.

Given the time lag between sea level change and the hydrothermal response, we can estimate melt migration rates if the depth at which melt originates is known. Assuming that the

average melt origin depth is 50 km (Key et al., 2013), we divide by the time elapsed between the maximum rate of sea level decrease and the maximum hydrothermal metal concentration/flux to estimate melt extraction velocity. For the last deglaciation we estimate melt migration rates ranging from 2.5 to 5 m/year, which is greater than the rate of >1 m/year that is estimated by U/Th disequilibrium in zero-age mid-ocean ridge basalts (Kelemen et al., 1997) and much less that the 50 m/year based on the time lag between deglaciation and volcanism in Iceland (Maclennan et al., 2002). Our results are consistent with recently published estimates from the EPR (Lund et al., 2016), suggesting a broad level of agreement amongst different EPR sites.

c) Pyroclastic Ash Layer in OC170-026-159 – 39°S

An unexpected pyroclastic ash layer was found in core OC170-026-159 from ~148-130 kyr BP (Figures 10 and 11). Recently published studies suggest that explosive submarine eruptions are more common than previously thought, with multiple ridge settings displaying evidence in the form of basaltic ash shards, rods, ribbons, limu o Pele, and other fluidal fragment morphologies (Clague, Paduan, and Davis, 2009). Pyroclastic glass shards, similar to those in core OC170-026-159, have been documented at the Juan de Fuca Ridge, Gorda Ridge, northern East Pacific Rise, and southern East Pacific Rise (Clague, Paduan, and Davis, 2009).

Pyroclasts are formed when ridge crest eruptions and hydrothermal plumes are abruptly introduced to cold seawater. The rapid quenching of magmatic CO_2 bubbles during this process creates pyroclastic debris. The pyroclastic debris is apparently carried upward and away from the eruption site by superheated plumes of rising seawater (Palmer and Ernst, 1998). Finer particles tend to travel farther from their source vents due to the slower settling rate of smaller

particles (Barreyre, Soule, and Sohn, 2011). Therefore, we expect to see larger grain sizes closer to the eruption site, with grain size gradually decreasing to very fine particles at more distal locations. Additionally, locations with higher eruption rates should have a greater abundance of pyroclasts based on the positive correlation with higher magmatic gas (CO_2) output (Lupton, Baker, and Massoth, 1999).

A study at the Escanaba segment of the Gorda Ridge measured basaltic glass mass per square meter to determine the dispersal of pyroclastic fragments from a hydrothermal vent site (Clague, Paduan, and Davis, 2009). Glass concentrations decreased from >2000 g/m^2 at the eruption site to <50 g/m^2 approximately 3 km away from the eruption fissure, indicating the dispersal distance is relatively limited. Additionally, the average mass of the largest three grains decreases away from the eruptive fissure, supporting the concept that finer particles are transported further from the source. A comprehensive analysis of 117 core locations within 5 km of the eruptive source can be used to assess the grain size distribution of ash deposits (Clague, Paduan, and Davis, 2009). Approximately ~41 % of the pyroclastic ash falls into the >500 μm size fraction (Figure 16, bottom panel). The percentages decrease as the diameter of the size fraction decreases, with 250-500 μm ~ 32 %, 125-250 μm ~20 %, and finally 63-125 μm < 7 %.

The ash layer in core OC170-026-159 was deposited when the core site was approximately 8-9 km from the ridge crest, about 5 km further from the source than any submarine ashes documented in the literature (Figure 11) (Clague, Paduan, and Davis, 2009). The ash particles at 140 kyr BP, which coincide with maximum TII concentrations, show an overall finer grain size distribution than the Gorda Ridge (Figure 16, top panel). About 47 % of the glass particles at 140 kyr BP fall within the 125-250 μm range, ~32 % in the 250-500 μm

class, ~17 % for 63-125 μm, and finally < 3 % for the >500 μm size grouping. The contrast in grain size distributions of the TII ash relative to the Gorda Ridge support the assertion that the dispersal pattern is unusually far from its source.

The size distribution comparisons between the OC170-026-159 TII ash and the Gorda Ridge glass data indicate that the submarine volcanic activity at 39°S may have been more explosive than baseline volcanic activity for this region. Whether the unusually far dispersal of ash was due to a larger eruption or more frequent eruptions, or enhanced lofting into the water column is unclear. In all likelihood, larger eruptions would likely create more pronounced plumes, so the two processes may have acted in concert to produce an ash layer 8-9 km from the ridge crest. Regardless, the abundance and morphology of the pyroclastic debris points to anomalous explosive volcanic activity on the PAR that coincided with Termination II. The presence of the pyroclastic ash layer is an unexpected and important discovery in that it is a direct indicator of anomalous release of heat and carbon from the mantle, suggesting a possible trigger for glacial terminations. Other ash layer discoveries at different locations along the PAR and other ridge crests would support this hypothesis.

d) Implication of Enhanced Hydrothermal Activity during Terminations: Geothermal Heat and Mantle Carbon Degassing

Our results show coordinated maxima in hydrothermal output and submarine volcanism during glacial terminations. If these processes are associated with anomalous mantle CO_2 and heat flux, they may act as a negative feedback on ice-sheet size (Lund and Asimow, 2011; Tolstoy, 2015). While estimates of modern carbon output from mid-ocean ridges are highly

uncertain (0.02 – 0.2 Pg C/year) (Cartigny et al., 2008), the carbon flux likely increased as a result of sea level modulation of mantle melting. Other carbon sources, including off-axis locations, back-arc basins, and island arcs, may contribute an additional 0.02-0.04 Pg C/year to the mid-ocean ridge carbon signal (Cartigny et al., 2008). Another study estimates that the global mid-ocean ridge mantle carbon flux ranges from 0.053- 0.091 Pg C/year (Huybers and Langmuir, 2009). However, the slow melt-migration rate for carbon-rich melts at mid-ocean ridges (~3 cm/year) may cause CO_2 emissions to lag sea level forcing by 60 kyr – the simulated minimum travel time of CO_2 through the melting regime (Burley and Katz, 2015). This implies that there may be substantial differences between the timing and amplitude of hydrothermal and carbon-flux variations.

In addition to mantle CO_2 flux acting as a negative feedback on ice-sheet size, hydrothermal heat itself may influence climate. Pollack et al. (1993) estimate that geothermal heat fluxes range from a background seafloor value of ~50 mW/m^2 to 350 mW/m^2 at mid-ocean ridges. Hofmann and Morales Maqueda (2009) use this estimate to create a model to determine the impact of geothermal heat fluxes on deep ocean circulation. Their results suggest that geothermal heat flux causes warming of waters below the main thermocline by 0.22-0.26°C, thereby eroding the deep ocean stratification. The excess heat is transported from the deep ocean and emerges along isopycnals into the surface Southern Ocean (Hofmann and Morales Maqueda, 2009). The introduction of buoyancy via geothermal heat drives enhanced circulation of Antarctic Bottom Water, which may release CO_2 stored in the abyss to the atmosphere, resulting in warmer temperatures and ice-sheet retreat. These ideas are speculative, however, and will require testing using proxies of mantle carbon input and deep ocean temperature.

5. Conclusion

The results presented here include oxygen stable isotope data and metal concentration records for two new sites along the SEPR and one on the PAR. The $\delta^{18}O$ data show MIS transition patterns consistent with the global benthic $\delta^{18}O$ stack of Lisiecki and Raymo (2005), indicating that sediments accumulate at the sites. Additionally, when tied to the benthic stack, the $\delta^{18}O$ data can be used to create age models for the cores. Peak metal concentrations for Fe, Mn, As, and V occur during Termination I for cores OC73-03-20 and OC170-026-159. The metal concentration maxima pattern also occurred during Termination II in cores Y71-07-53 and OC170-026-159. MAR-based metal flux patterns for cores Y71-07-53 and OC170-026-159 display similar patterns of maximum metal values during Terminations I and II. The coherence between the metal concentration and MAR-based data indicate that dilution from non-hydrothermal components is not a primary driver of the Fe and Mn peaks.

Our finding of peak metal fluxes during glacial terminations support the recently published records of hydrothermal activity at sites further north along the EPR (Lund et al., 2016). A comparison of MAR-based metal fluxes from Y71-07-53 to ^{3}He-based metal fluxes from a core at 11°S from Lund et al. (2016) indicates a similar pattern of maximum fluxes during Termination I. The agreement between these two flux methods confirms the overall reliability of the MAR-based flux data for core Y71-07-53 based on the rough doubling of ^{3}He flux values from the LGM to TI. Qualitative flux data from core OC170-026-159 also recorded a doubling of values during the LGM to TI, suggesting that the Pacific Antarctic Ridge experiences similar hydrothermal activity patterns over glacial-interglacial cycles. However, ^{3}He data are necessary to fully and accurately quantify fluxes cores OC170-026-159 and OC73-03-20.

Diagenetic overprinting can complicate the interpretation of Fe and Mn records in marine sediments. It is unlikely that diagenesis is a first order driver of the peaks in cores Y71-07-53, OC73-03-20, and OC170-026-159, for several reasons, however. The core sites represent varied background redox conditions due to a decreasing north-south gradient in biogenic opal and organic carbon concentrations. Sites located further from the highly productive equatorial Pacific have decreasing organic carbon concentrations that are exported to underlying seafloor sediments. While it is possible that some suboxic Mn diagenesis occurred in core Y71-07-53, low organic carbon levels at all three core locations prevent the remobilization of Fe. The hierarchy of oxidants in the pore water profiles indicates that Fe oxyhydroxides and Mn oxides should be deposited at different depths if they have been affected by diagenesis. However, we observe contemporaneous Fe and Mn peaks in each sediment core spanning Terminations I and II, suggesting that diagenesis is not a primary driver of coordinated Fe and Mn maxima. Finally, the down core Fe/Mn ratio measured in the three core locations falls within 2σ of the hydrothermal end member from core tops determined by Dymond (1981). Overall, these lines of evidence suggest that diagenesis is not a primary driver of the Fe and Mn signal found at the SEPR and PAR.

The ~10 cm thick pyroclastic ash layer at 39°S includes basalt pieces that are both fluidal and shard-like, with limu o Pele forms ranging from bubble-wall fragments to ribbons and rods. The fluidal morphology of the pyroclastic glass shards matches descriptions from other mid-ocean ridges (Clague, Paduan, and Davis, 2009), suggesting that submarine activity was responsible for the Termination II ash. The median grain size of the basaltic ash layer is finer than that at other ridge locations, indicating that the ash traveled further from the eruption

source. This was possibly due to larger or more frequent eruptions, or enhanced lofting of plumes into the water column. The discovery of the pyroclastic ash layer at 39°S is important because it is a direct product of submarine explosions at the PAR. It is recorded in the sediment core as a ~10x increase in Ti and Al concentrations during TII, which are two elements not affected by diagenesis or remobilization by organic matter in the sediment column. The timing of the ash layer coincides with the maximum Fe and Mn peaks during TII (within error, ± 3 kyr), suggesting that submarine volcanism and hydrothermal activity were responsible for these patterns. Therefore, the presence of a pyroclastic ash during TII likely suggests that hydrothermal activity and submarine volcanism are the drivers of peak hydrothermal metal concentrations and fluxes during terminations, not diagenesis.

Although the mechanistic link between mid-ocean ridge magmatism and glacial terminations is still unknown, the data presented here suggest the two are related. To further demonstrate that the solid earth-climate mechanism is linked, additional mid-ocean ridge settings must be explored through comprehensive, multi-proxy records. Ridges that are sensitive to mantle carbon and geothermal inputs will provide the most compelling results. Modeling investigations using these inputs will help uncover their impact on abyssal ocean circulation and mixing. The coherent timing between enhanced hydrothermal and submarine volcanic activity and glacial terminations on the SEPR and PAR imply that the two processes are linked. Possible climate implications from enhanced volcanic activity are a less stratified deep ocean, more rapid cycling of Antarctic Bottom Water, and release of CO_2 from the deep ocean to the atmosphere.

APPENDIX

PLOTS OF THE DATA

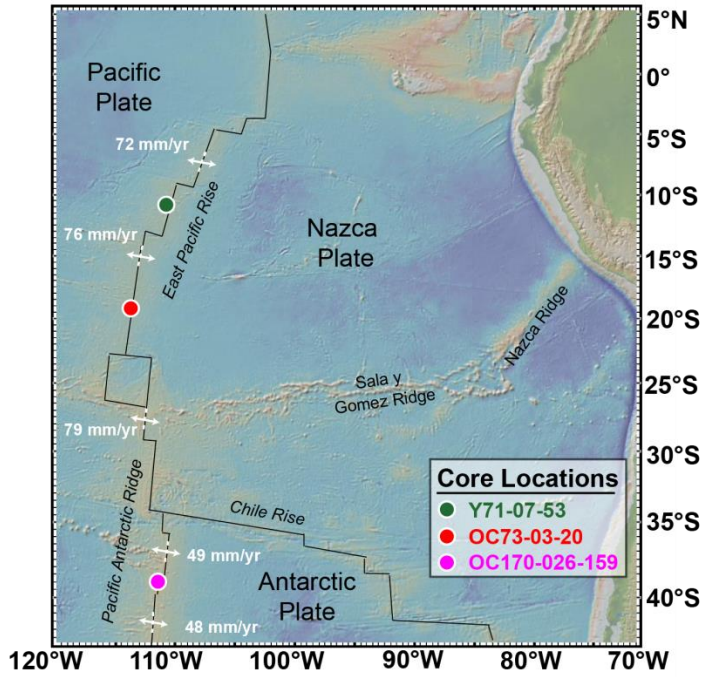

Figure 1. The study area and location of the three core sites. Core locations include 11°S (Y71-07-53 in green), 19°S (OC73-03-20 in red), and 39°S (OC170-026-159 in purple). See Table 1 for exact locations. Half-spreading rates are shown in white (http://www.ldeo.columbia.edu/users/menke/plates.html). The map was generated using GeoMappApp (www.geomapapp.org).

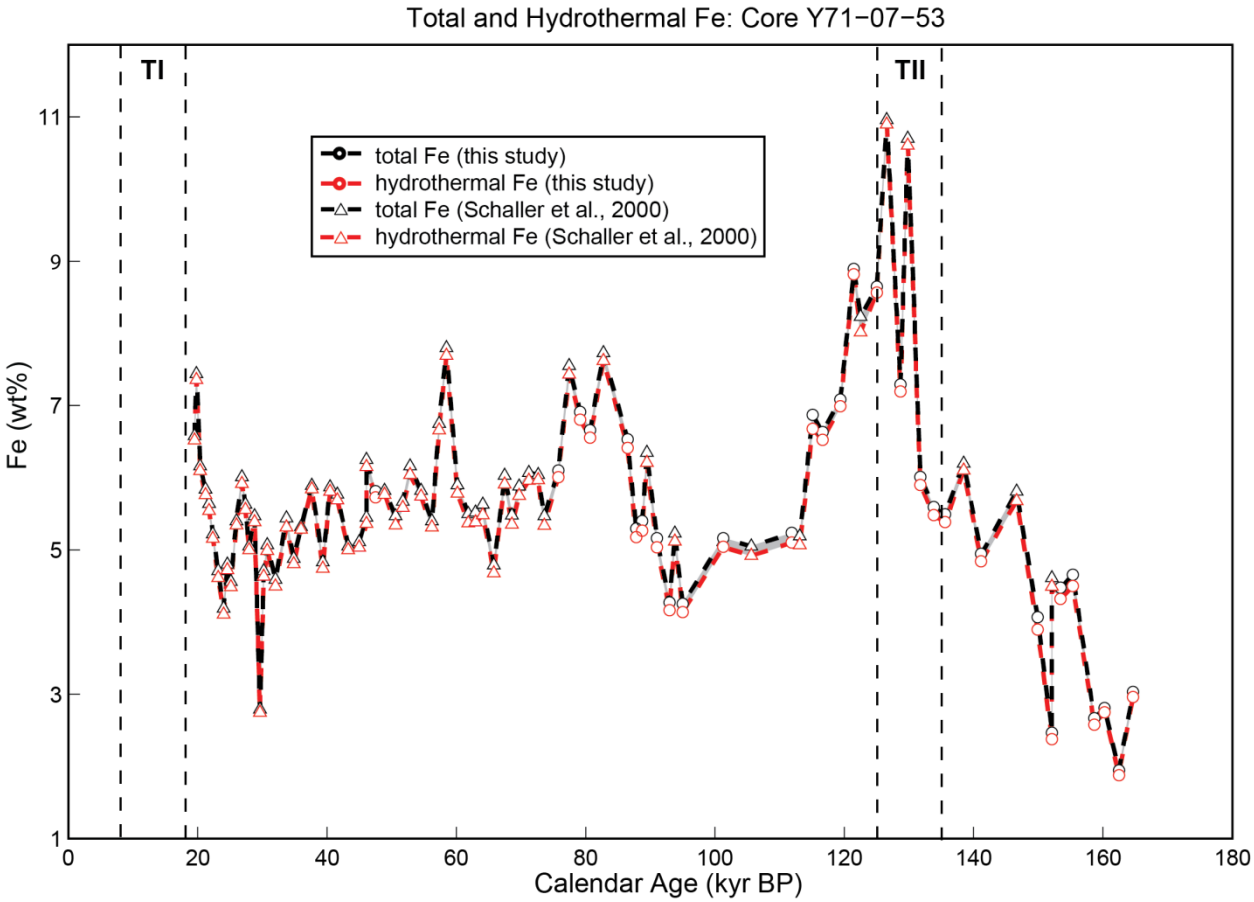

Figure 2. Total Fe and hydrothermal Fe for core Y71-07-53. The difference between the total Fe (black) and the hydrothermal Fe (red) curves represents the detrital correction, which in this case is negligible. The detrital Fe contribution was determined by multiplying the Ti concentration of each sample by the Fe/Ti ratio of recent EPR basalts (8.1 ± 0.3) (Schramm et al., 2005). A similar approach was used for calculating hydrothermal Mn using the Mn/Ti ratio of the same EPR basalts (0.1 ± 0.01). These results are not shown because the corrections were minimal (< 0.003 %). Vertical dashed lines delineate Terminations I (TI) and II (TII). Circles represent data from this study, while triangles represent data from Schaller et al. (2000).

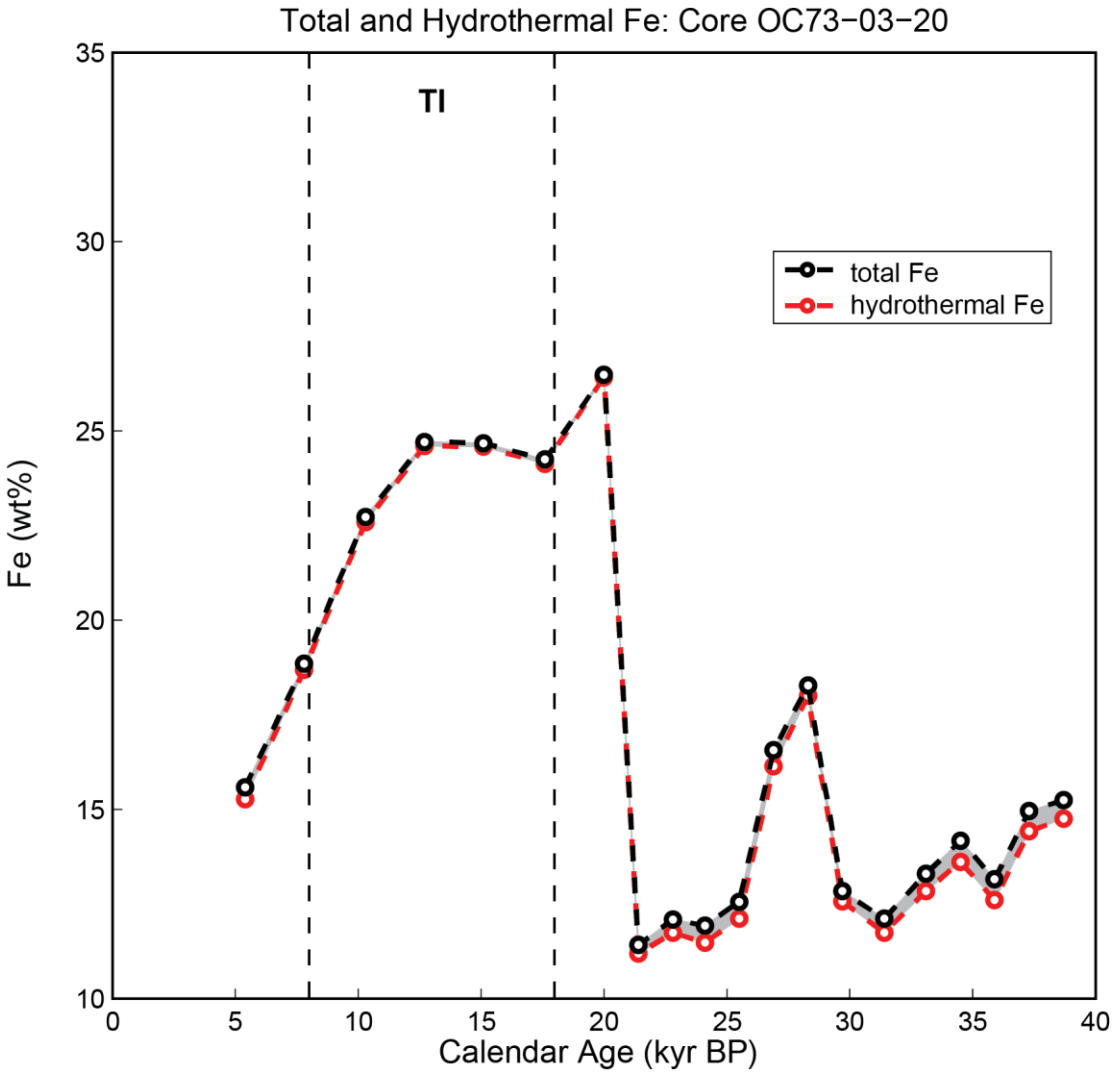

Figure 3. Total Fe and hydrothermal Fe for core OC73-03-20. Plotting convention is the same as Figure 2. Note that hydrothermal Fe reaches 25% of the bulk sediment weight during TI (vertical dashed lines). Manganese results are not shown because the corrections were minimal (< 0.007 %).

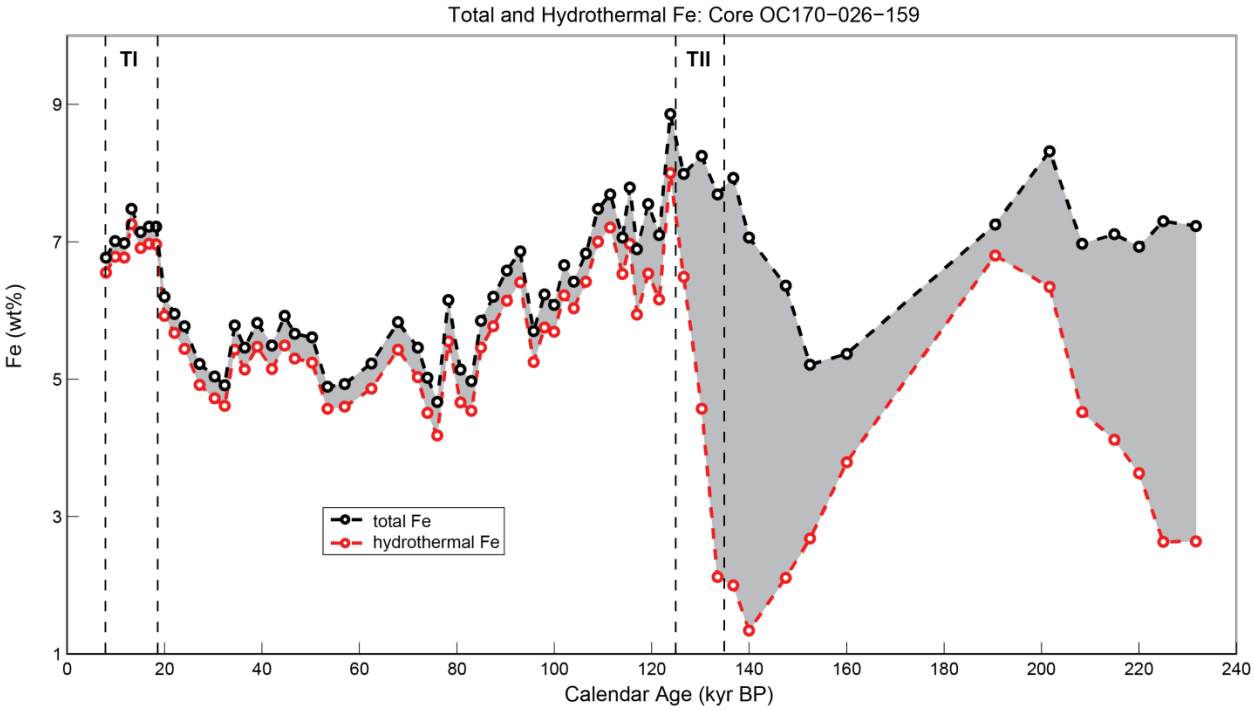

Figure 4. Total Fe and hydrothermal Fe for core OC170-026-159. Plotting convention is the same as Figure 1. Unlike cores Y71-07-53 and OC73-02-20, the detrital correction (gray area) was a substantial fraction of the total Fe due to the input of basaltic ash (see Figures 10 and 11). Again, Mn results are not shown because the detrital corrections were minimal (< 0.082 %).

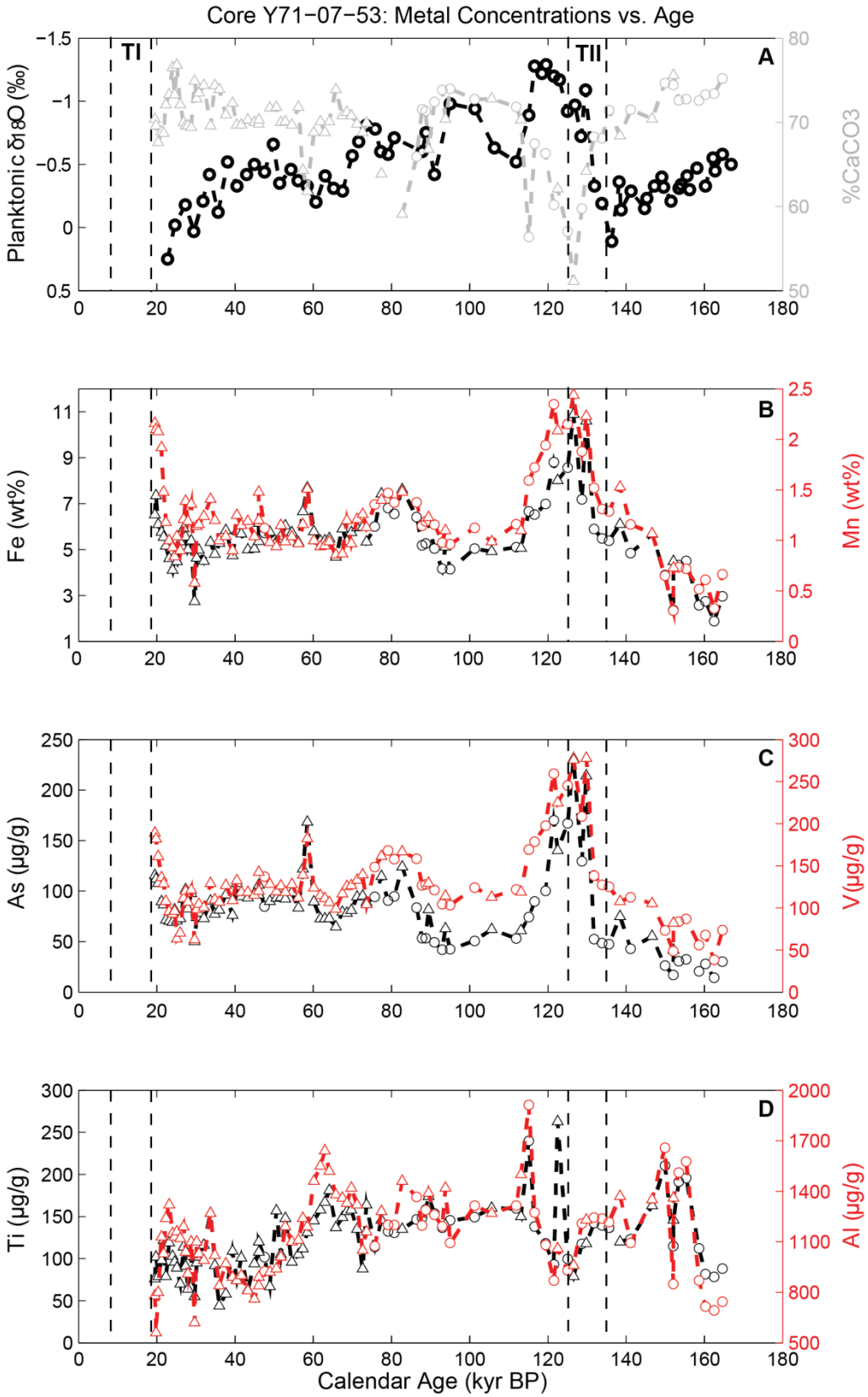
Core Y71−07−53: Metal Concentrations vs. Age
TI
TII
A
Planktonic δ18O (‰)
%CaCO3
B
Fe (wt%)
Mn (wt%)
C
As (µg/g)
V(µg/g)
D
Ti (µg/g)
Al (µg/g)
Calendar Age (kyr BP)

Figure 5. Results for core Y71-07-53, including A) G. *ruber* $\delta^{18}O$ (black circles) (‰) and $\%CaCO_3$ (gray), B) Fe (black) and Mn (red) concentrations (wt %), C) As (black) and V (red) concentrations (μg/g), and D) Ti (black) and Al (red) concentrations (μg/g). Both Fe and Mn concentrations have been corrected for detrital input from basaltic debris (see Methods). Terminations I and II are outlined in black dashed lines. Maximum Fe, Mn, As, and V concentrations coincide approximately with TII. The metal concentration data is a combination of metal concentration and $\%CaCO_3$ data from this study (circles) and from Schaller et al. (2000) (triangles).

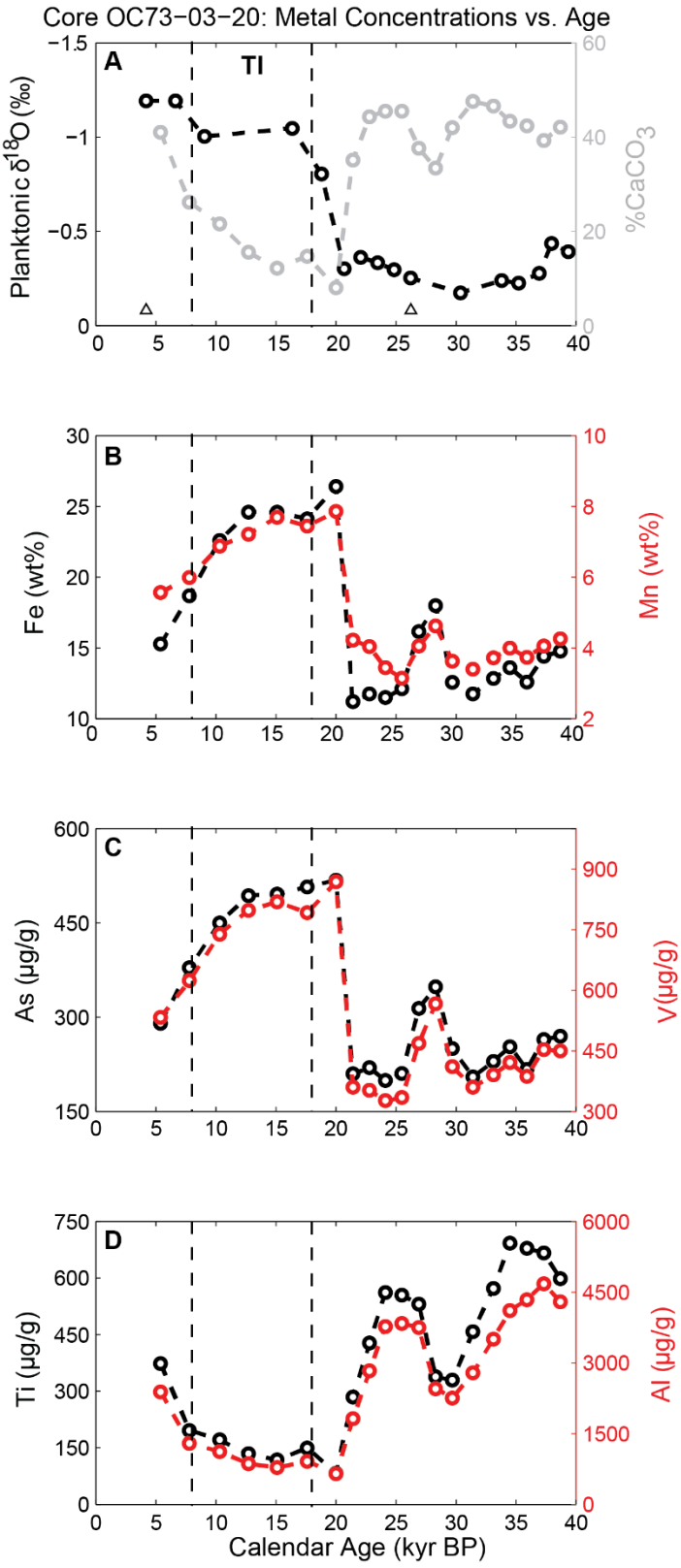
Core OC73−03−20: Metal Concentrations vs. Age
A
TI
Planktonic δ18O (‰)
%CaCO3
B
Fe (wt%)
Mn (wt%)
C
As (µg/g)
V(µg/g)
D
Ti (µg/g)
Al (µg/g)
Calendar Age (kyr BP)

Figure 6. Results for core OC73-03-20, including A) G. *ruber* $\delta^{18}O$ (black circles) (‰) and $\%CaCO_3$ (gray circles), B) Fe (black circles) and Mn (red circles) concentrations (wt %), C) As (black circles) and V (red circles) concentrations (μg/g), and D) Ti (black circles) and Al (red circles) concentrations (μg/g). Fe and Mn have been corrected for detrital input from basalt debris (see Methods). Average maximum concentrations occur during Termination I (TI) (black dashed lines). Two calendar-corrected radiocarbon ages for this core are indicated by black triangles at 4.2 kyr BP and 27.6 kyr BP in panel A (see Methods).

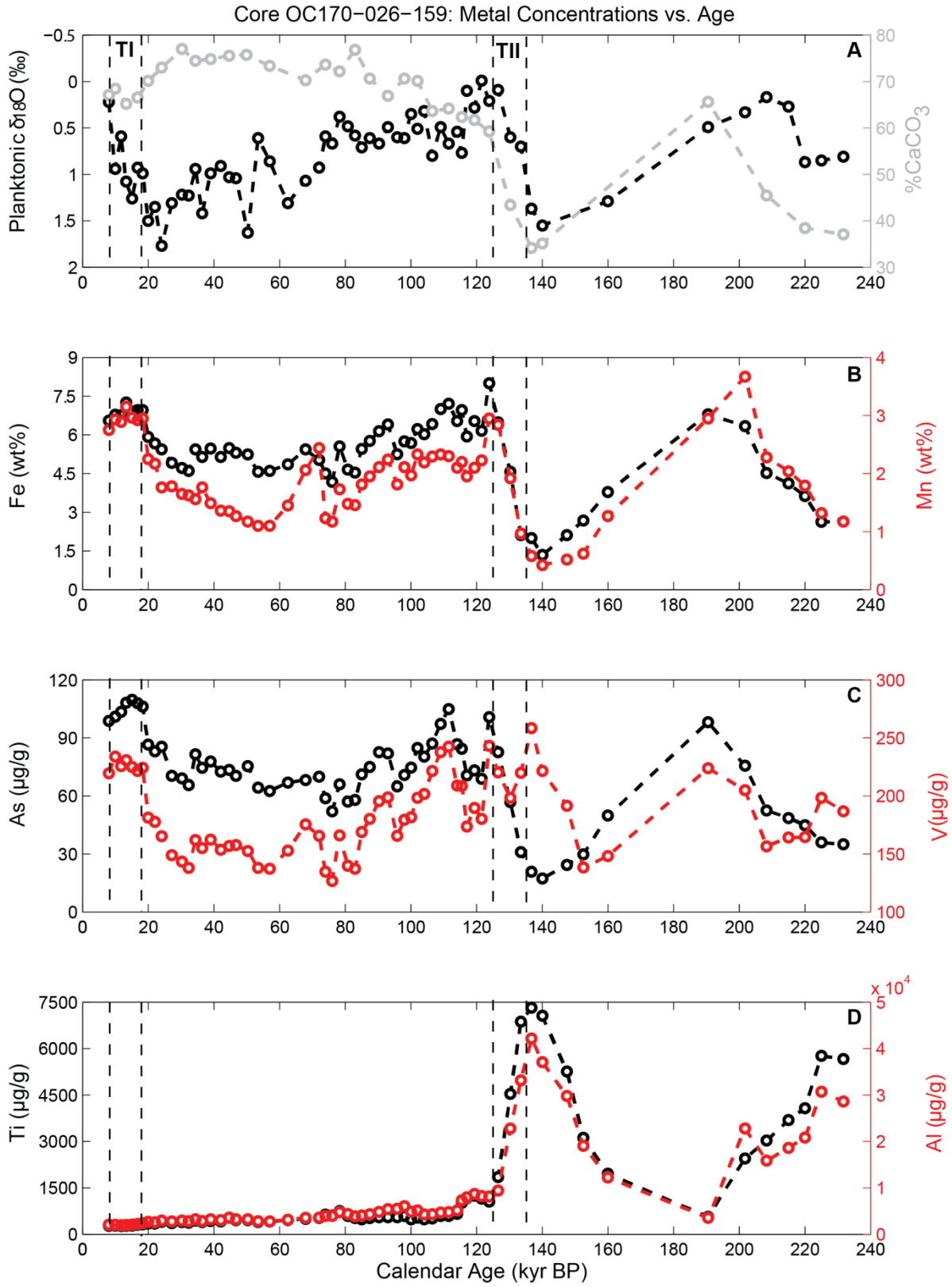
Core OC170−026−159: Metal Concentrations vs. Age
TI
TII
A
Planktonic δ18O (‰)
%CaCO3
B
Fe (wt%)
Mn (wt%)
C
As (µg/g)
V(µg/g)
D
Ti (µg/g)
Al (µg/g)
x 10^4
Calendar Age (kyr BP)

Figure 7. Results for core OC170-026-159, including a) G. *ruber* $\delta^{18}O$ (black circles) (‰) and $\%CaCO_3$ (gray circles), b) Fe (black circles) and Mn (red circles) concentrations (wt %), c) As (black circles) and V (red circles) concentrations (μg/g), and d) Ti (black circles) and Al (red circles) concentrations (μg/g). Fe and Mn have been corrected for detrital input from basaltic debris (see Methods). Maximum metal concentrations occur during Terminations I (TI) and II (TII), and persist into MIS 5e (130-117 kyr) (black dashed lines). Note that high Ti and Al concentrations occur at the end of MIS 6 and during TII.

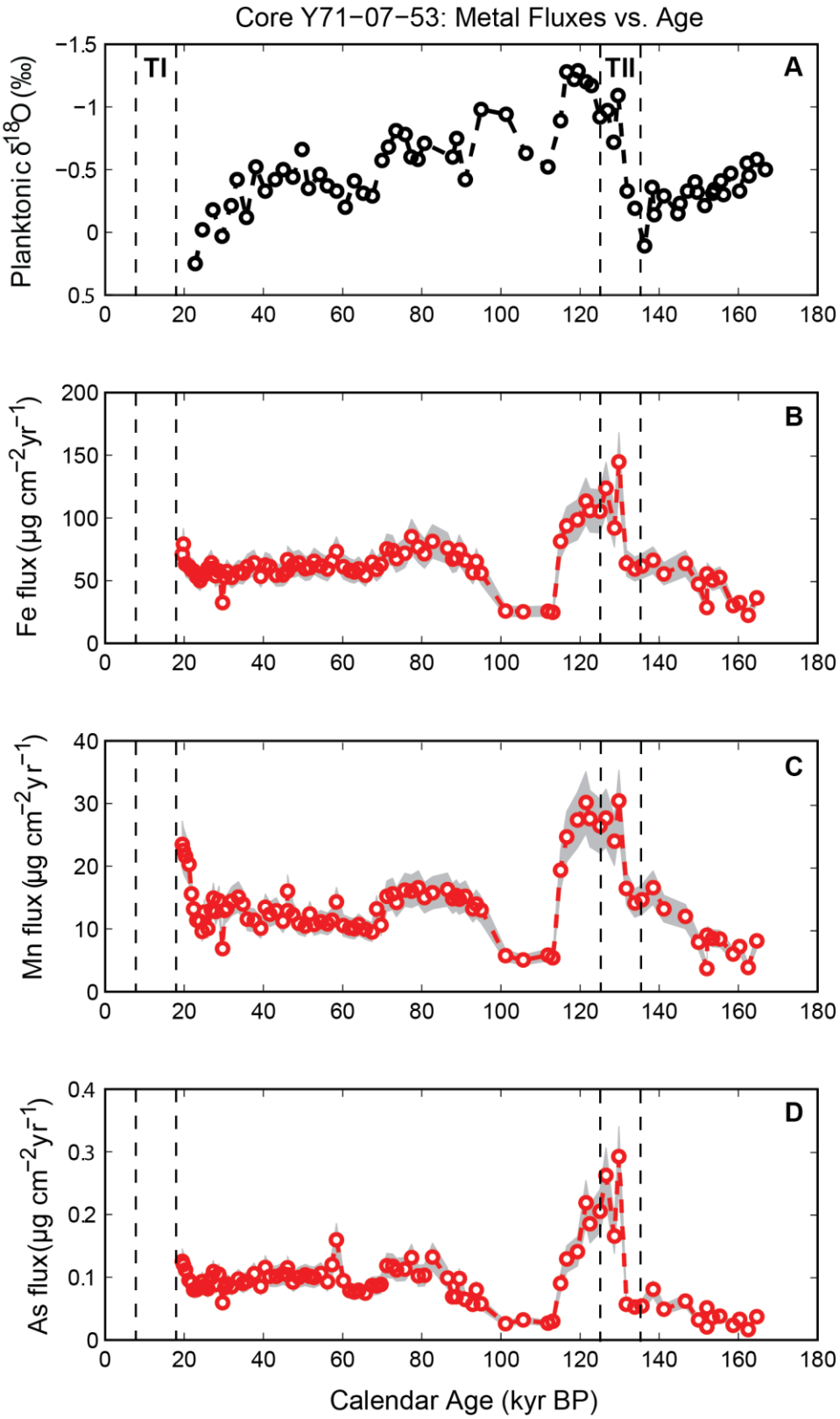
Core Y71−07−53: Metal Fluxes vs. Age
TI
TII
A
B
C
D
Planktonic δ18O (‰)
Fe flux (µg cm−2yr−1)
Mn flux (µg cm−2yr−1)
As flux (µg cm−2yr−1)
Calendar Age (kyr BP)

Figure 8. Metal fluxes vs. age (kyr BP) for core Y71-07-53. A) G. *ruber* $\delta^{18}O$, B) Fe flux, C) Mn flux, and D) As flux. Maximum fluxes occur during Termination II (black dashed lines) and persist into MIS 5e (132-120 kyr BP). Error bars (gray shaded area) reflect the uncertainty of the flux estimates (see Methods).

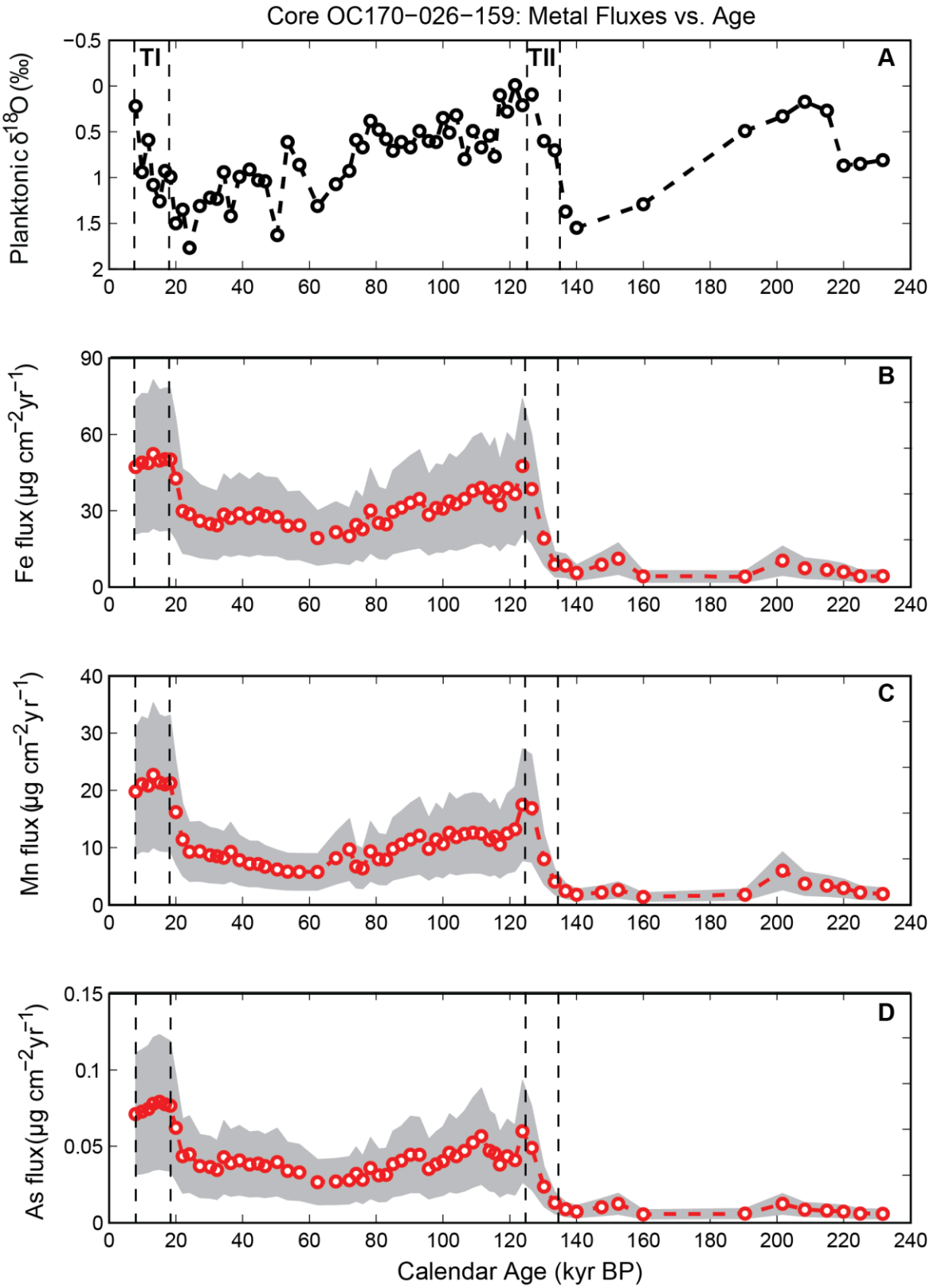
Core OC170−026−159: Metal Fluxes vs. Age
TI
TII
A
B
C
D
Planktonic δ18O (‰)
Fe flux (µg cm−2yr−1)
Mn flux (µg cm−2yr−1)
As flux(µg cm−2yr−1)
Calendar Age (kyr BP)

Figure 9. Metal fluxes for core OC170-026-159. A) G. *ruber* $\delta^{18}O$, B) Fe flux, C) Mn flux, and D) As flux. Maximum fluxes occur during Terminations I (TI) and II (TII) (black dashed lines). Error bars (gray shaded area) reflect the uncertainty of the flux estimates (see Methods). There is a clear shift from low fluxes prior to 140 kyr BP to generally higher fluxes afterward. The primary driver of the step change in flux is the ~3x increase in sedimentation rate from MIS 6 to MIS 5e.

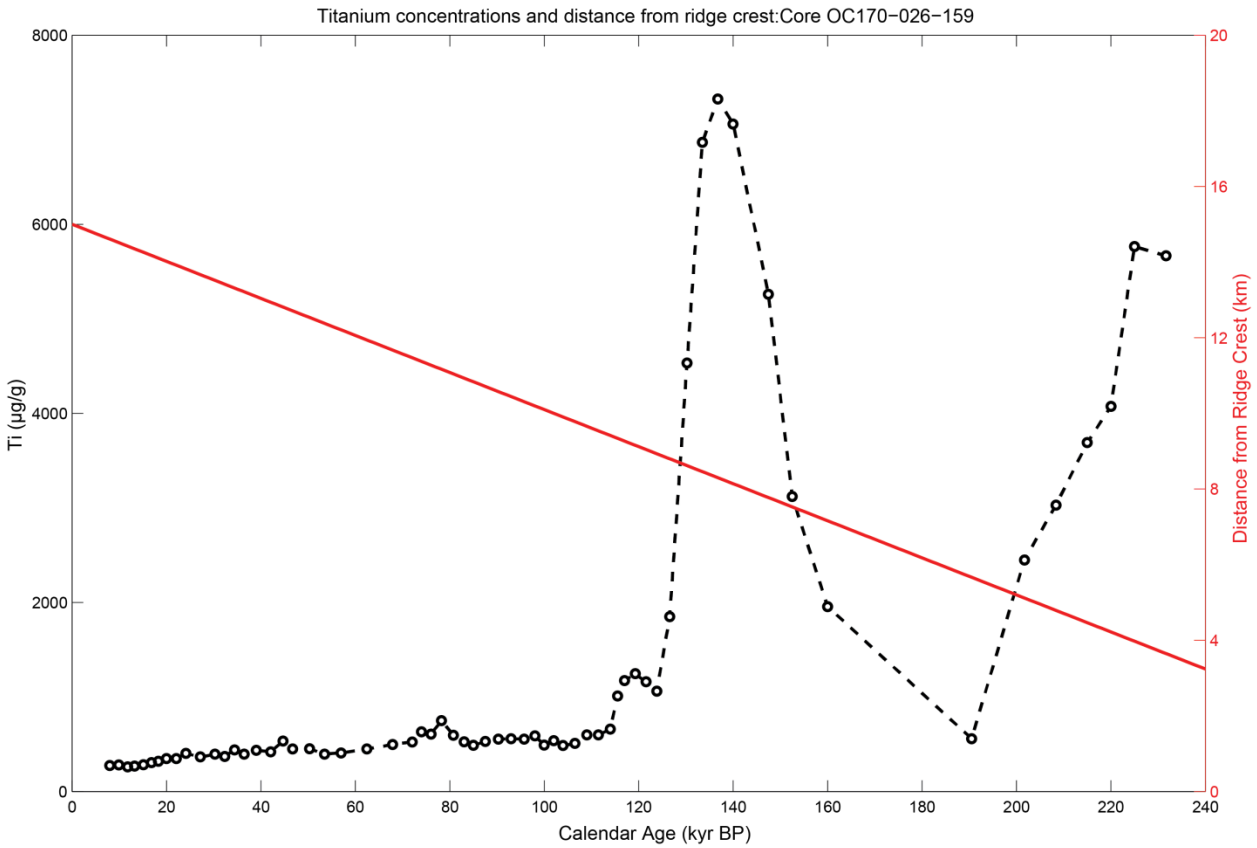

Figure 10. Titanium concentrations (µg/g) for core OC170-026-159 (black circles) and core distance (km) from the ridge crest vs. age (kyr BP) (red), assuming a half-spreading rate of 49 mm/year (http://www.ldeo.columbia.edu/users/menke/plates.html). Peak Ti concentrations occur during two intervals, one when the core was 8-9 km from the ridge crest, and one when the core was within approximately 4 km of the ridge crest. High Ti concentrations coincide with intervals of abundant basaltic glass (Figure 11).

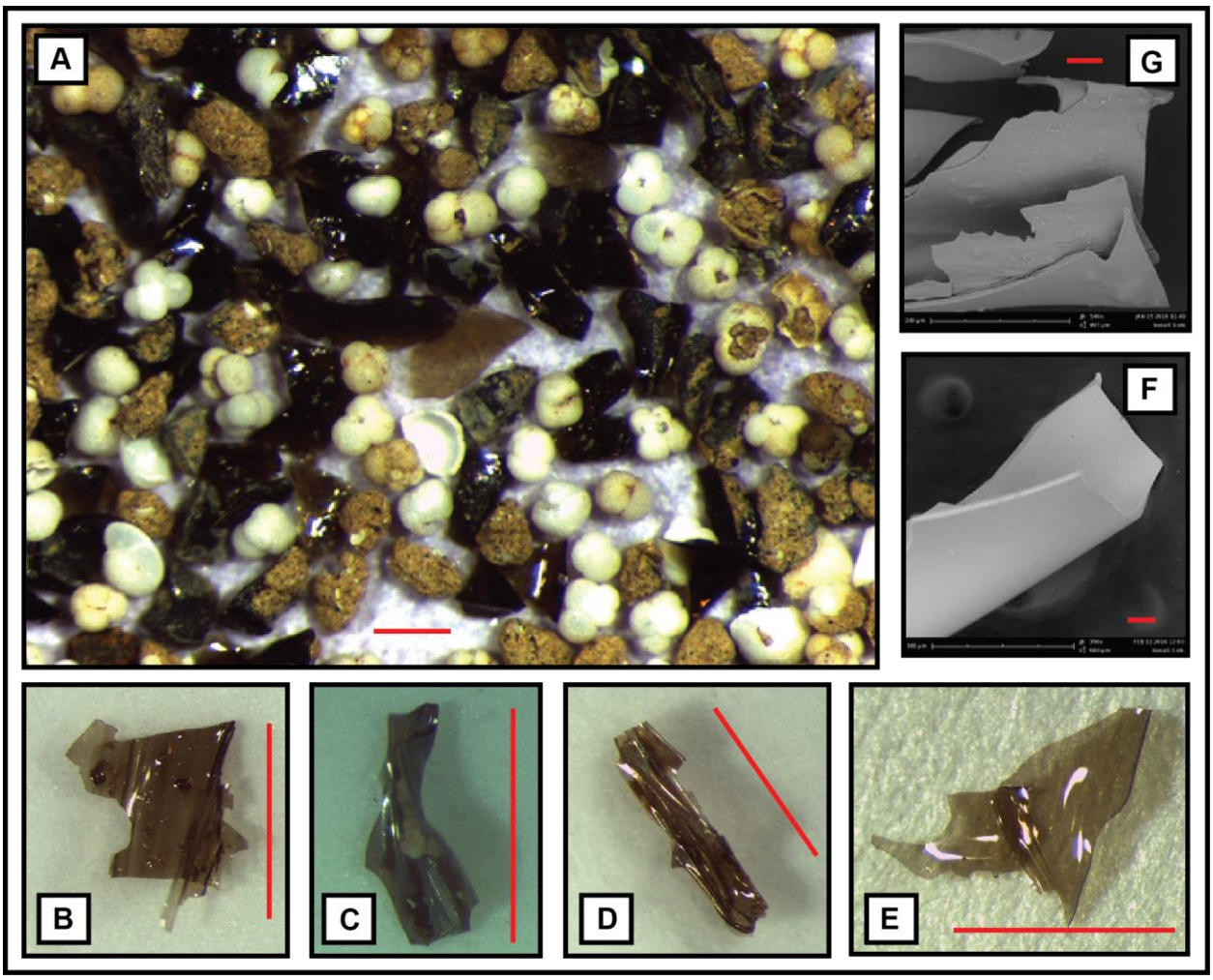

Figure 11. Photographs and SEM images of basaltic ash debris in core OC170-026-159. A) Image of sample from 132 cm (~140 kyr BP) including foraminifera and ash from the 250-500 μm size fraction, B) bubble-walled limu o Pele fragment, C & D) rod structures (folded and twisted), E) ribbon (folded), and F & G) SEM pictures of a folded ribbon piece and a curved ribbon piece. The red scale lines are 250 μm.

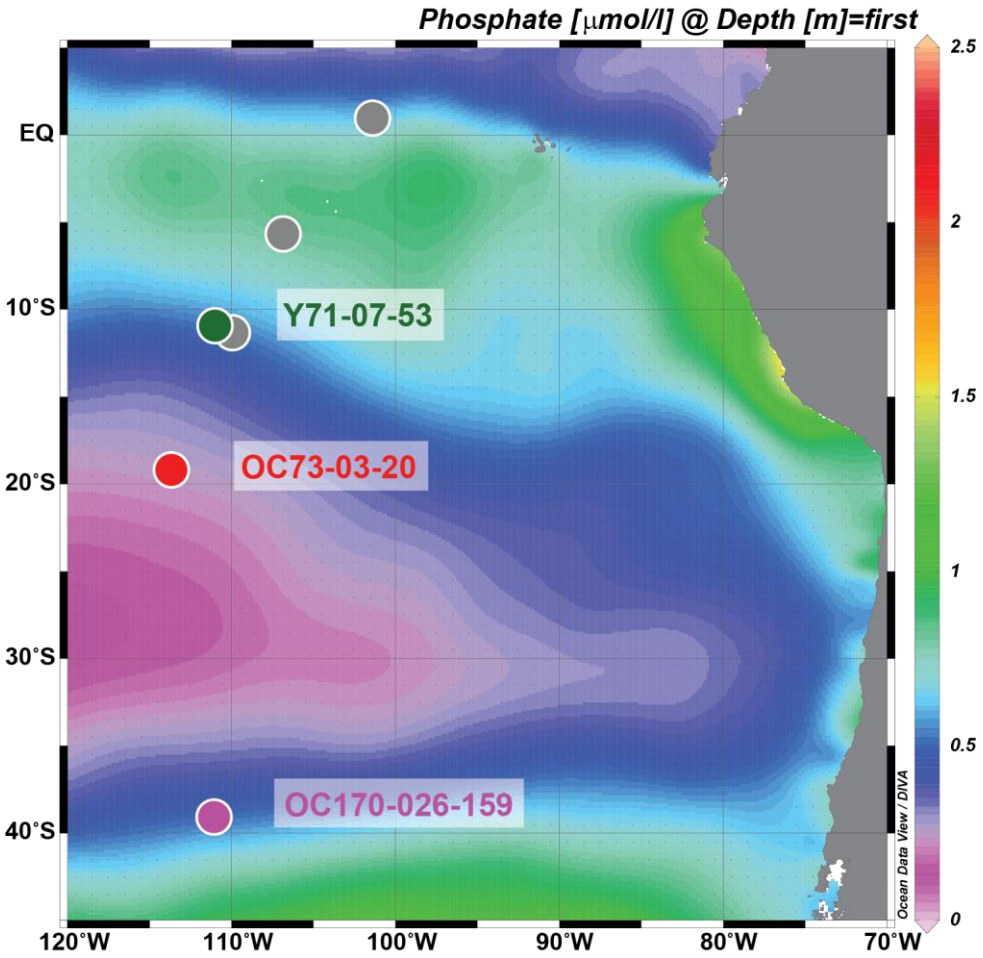

Figure 12. The location of the three core sites superimposed on a map of surface ocean phosphate concentrations. Core locations include 11°S (Y71-07-53 in green), 19°S (OC73-03-20 in red), and 39°S (OC170-026-159 in purple). Also shown in gray are the cores sites at 1°N, 6°S, and 11°S reported in Lund et al. (2016). Phosphate concentrations (µmol/L) provide a qualitative indicator of export production to the underlying sediments. The map was generated with World Ocean Atlas (2013) data using Ocean Data View (www.odv.org).

Figure 13. Images of the working (top) and archive (bottom) halves of core Y71-07-53 for the depth interval 150-200 cm (~112-130 kyr BP). Age control points are inferred from the MIS 6/5 transition (130 kyr BP) and the transition between the MIS 5e and 5d peaks (~115 kyr BP) (red lines). The mottled appearance is due to bioturbation from the metal-rich interval (170 to 200 cm) downward. Core Y71-07-53 was sampled multiple times over the course of ~20 years, with varying sample intervals taken from both the working and archive halves (Schaller et al., 2000). Given the core heterogeneity, the associated metal concentrations will depend on whether the sampling interval coincided with a bioturbated interval. Photographs are courtesy of the Oregon State University Marine Geology Repository (http://osu-mgr.org/).

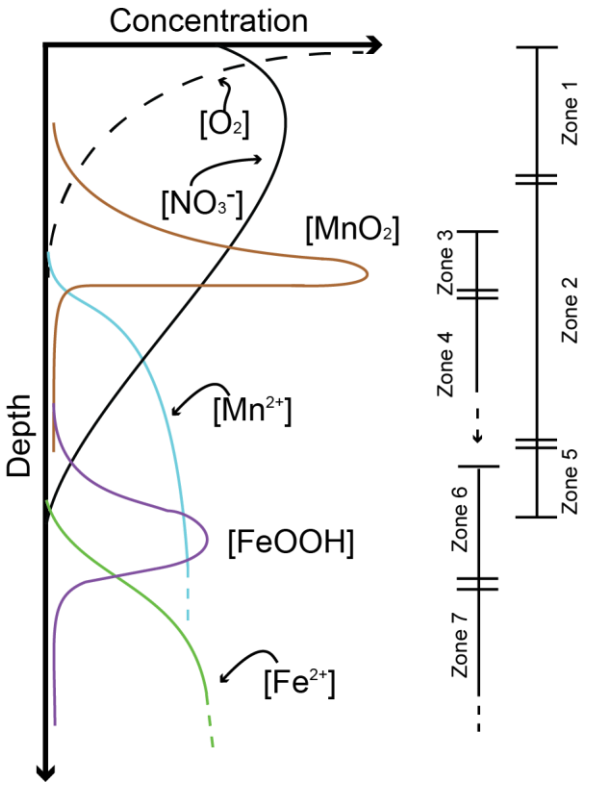

Figure 14. Schematic diagram of pore water profiles for Fe and Mn. Depth and concentration axes are in arbitrary units. The relative depths of the MnO_2 and FeOOH precipitates are dependent on the hierarchy of oxidants: O_2 (black dashed) > MnO_2 (brown) ~ NO_3^- (black solid) > FeOOH (purple) > SO_4^{2-}(not shown). Mn(II) (cyan) and Fe(II) (green) are also shown. The zones and concentration variability are discussed in the text.

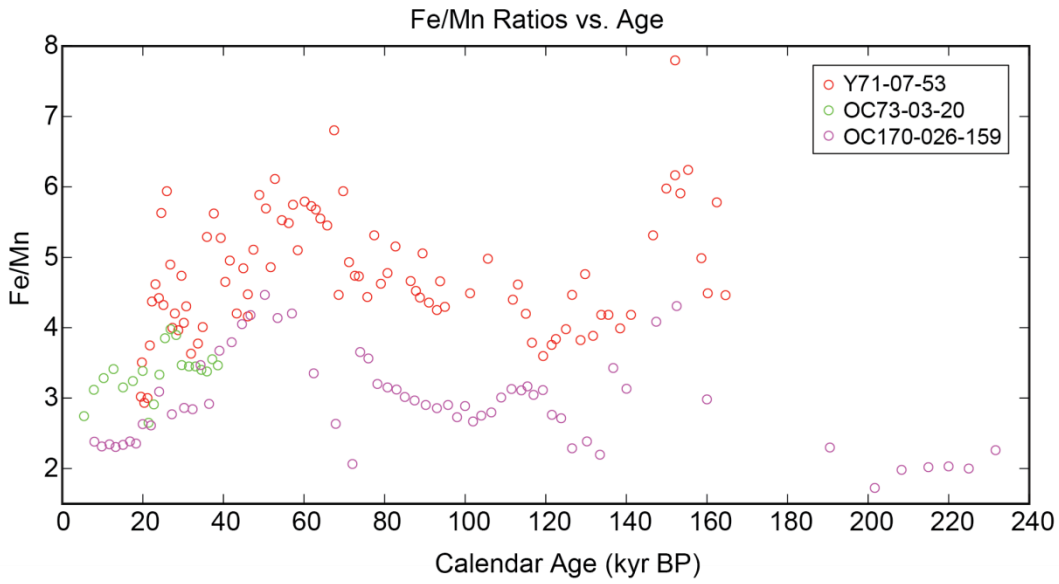

Figure 15. Fe/Mn ratios vs. age (kyr BP) for cores Y71-07-53 (11°S, green circles), OC73-03-20 (19°S, red circles), and OC170-026-159 (39°S, purple circles). The 11°S samples average 4.8 ± 0.85 (1□). Higher Fe/Mn ratios from 160-150 kyr BP and from 70 to 20 kyr BP may be due to Mn remobilization. Samples at 19°S average 3.5 ± 0.34 (1□), which is very similar to the estimated Fe/Mn ratio for hydrothermal sediments along the EPR (3.5 ± 0.9 (1□)) (Dymond, 1981). Samples at 39°S average 2.9 ± 0.65 (1□), which is lower than the Fe/Mn end member for EPR ridge crest sediments. Note that this core is from the Pacific Antarctic Ridge where the hydrothermal endmember is unconstrained.

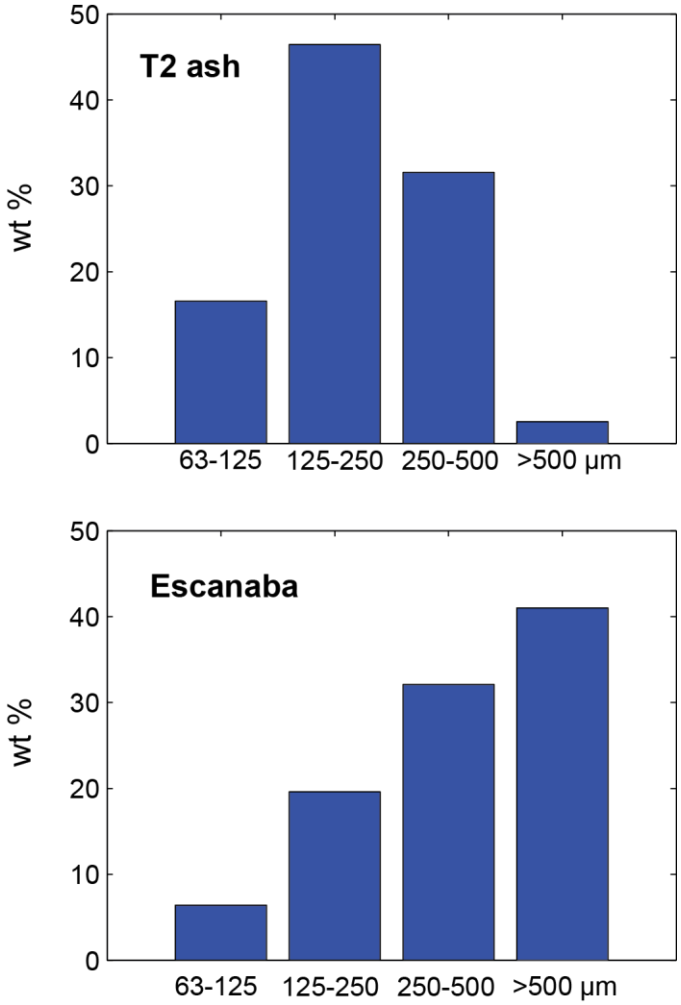

Figure 16. Grain size distribution of basaltic ash pieces from Termination II (~148-130 kyr BP) (top) and from the Escanaba segment of the Gorda Ridge (~42°N, 127°W) (bottom) (Clague, Paduan, and Davis, 2009). Size fractions are divided into four classes: 63-125 µm, 125-250 µm, 250-500 µm, and > 500 µm. The TII ash from core OC170-026-159 is dominated by the 125-250 µm size fraction, while the Gorda Ridge samples are skewed towards coarser grain sizes.

TABLES OF METAL CONCENTRATIONS AND FLUXES

Table 3: Bulk sediment element concentrations from core Y71-07-53 (11°S). Metal concentration data is a collaboration of analyses from this study and from Schaller et al. (2000).

Depth (cm)	Age (kyr BP)	$CaCO_3$ (%)	Mo (ug/g)	Al (ug/g)	Ca (ug/g)	Ti (ug/g)	V (ug/g)	Cr (ug/g)	Mn (ug/g)	Fe (ug/g)	Ni (ug/g)	Cu (ug/g)	Zn (ug/g)	As (ug/g)	Mn (wt %)*	Fe (wt %)*	Fe/Mn (wt %)
0.25	19.5	70.4	13.83	780.0		76.0	189.0	25.8	21600	65800				115.5	2.16	6.52	3.0
0.75	19.8	69.6	12.02	560.0		102.0	182.1	24.3	21000	74400				112.0	2.10	7.36	3.5
1.75	20.4	67.6	8.42	800.0		79.0	161.1	17.8	20800	61600				107.8	2.08	6.10	2.9
3.25	21.2	68.9	5.99	1130.0		98.0	136.1	14.5	19200	58400				89.6	1.92	5.76	3.0
4.25	21.8	68.7	2.60	1030.0		122.0	128.8	19.5	14800	56400				86.5	1.48	5.54	3.7
5.25	22.3	72.1	1.99	1240.0		79.0	108.0	11.9	11800	52200				71.4	1.18	5.16	4.4
6.75	23.2	73.3	1.81	1320.0		119.0	95.8	13.6	10000	47100				70.3	1.00	4.61	4.6
8.25	24.0	76.5	1.67	1150.0		103.0	92.8	12.8	9300	41900				69.2	0.93	4.11	4.4
9.25	24.6	73.3	1.32	1130.0		96.0	96.1	24.9	8400	48000				81.5	0.84	4.72	5.6
10.25	25.1	76.8	2.26	1160.0		89.0	63.4	15.3	10400	45600				70.6	1.04	4.49	4.3
11.75	26.0	72.1	1.56	1120.0		70.0	70.2	20.0	9000	54000				73.0	0.90	5.34	5.9
13.25	26.8	70.0	1.72	1190.0		114.0	111.5	17.2	12100	60100				92.0	1.21	5.92	4.9
14.25	27.4	69.6	2.03	1040.0		91.0	120.1	15.3	13900	56300				101.7	1.39	5.56	4.0
15.25	28.0	69.6	2.06	910.0		64.0	106.9	14.4	11900	50500				82.5	1.19	5.00	4.2
16.75	28.8	69.4	1.96	1100.0		103.0	121.3	14.9	13600	54700				97.7	1.36	5.39	4.0
18.25	29.6	74.9	0.91	620.0		55.0	62.4	12.2	5800	27900				50.3	0.58	2.75	4.7
19.25	30.2	72.8	1.70	1100.0		95.0	98.2	11.0	11400	47100				74.0	1.14	4.63	4.1
20.25	30.8	73.5	1.82	1030.0		102.0	104.5	15.1	11600	50700				78.2	1.16	4.99	4.3
22.50	32.0	74.4	1.69	990.0		116.0	100.5	13.7	12400	45900				73.1	1.24	4.50	3.6
25.50	33.7	69.6	2.19	1270.0		154.0	129.1	19.2	14100	54400				90.3	1.41	5.32	3.8
27.50	34.8	74.4	1.70	1020.0		92.0	109.8	15.5	12000	48800				77.3	1.20	4.81	4.0
29.50	36.0	73.9	1.63	840.0		44.0	107.0	21.4	10000	53200				81.2	1.00	5.28	5.3

Depth (cm)	Age (kyr BP)	$CaCO_3$ (%)	Mo (ug/g)	Al (ug/g)	Ca (ug/g)	Ti (ug/g)	V (ug/g)	Cr (ug/g)	Mn (ug/g)	Fe (ug/g)	Ni (ug/g)	Cu (ug/g)	Zn (ug/g)	As (ug/g)	Mn (wt %)*	Fe (wt %)*	Fe/Mn (wt %)
32.50	37.7	70.9	1.71	970.0		58.0	126.8	24.1	10400	58900				96.3	1.04	5.84	5.6
35.50	39.3	72.3	1.36	890.0		109.0	108.8	41.7	9000	48300				76.2	0.90	4.74	5.3
37.50	40.5	69.7	1.69	870.0		75.0	132.6	27.3	12500	58700				107.7	1.25	5.81	4.7
39.50	41.6	69.7	1.73	900.0		101.0	118.6	25.8	11500	57700				94.7	1.15	5.69	5.0
42.50	43.3	70.3	1.66	810.0		63.0	118.7	26.2	11900	50500				93.4	1.19	5.00	4.2
45.50	45.0	70.0	1.60	760.0		94.0	115.4	32.8	10400	51100				97.6	1.04	5.03	4.8
47.50	46.1	69.8	1.60	890.0		108.0	120.0	25.3	12000	54500				96.3	1.20	5.36	4.5
47.50	46.1	70.3	2.88	840.0		120.0	142.6	31.9	14800	62500				106.1	1.48	6.15	4.2
50.00	47.5		1.78	924.3	295199	101.6	137.3	25.5	11226	58122	76.6	219.8	114.6	84.7	1.12	5.73	5.1
52.50	48.9	71.7	1.45	920.0		67.0	128.3	60.3	9800	58200				89.9	0.98	5.77	5.9
55.50	50.6	71.8	1.40	940.0		157.0	119.5	35.7	9400	54700				93.1	0.94	5.34	5.7
57.50	51.7	70.0	1.37	1010.0		105.0	126.4	31.1	11500	56700				93.7	1.15	5.58	4.9
59.50	52.8	70.1	1.43	1190.0		148.0	118.6	31.5	9900	61600				92.3	0.99	6.04	6.1
62.50	54.5	69.7	1.41	1100.0		96.0	128.1	36.3	10400	58200				98.6	1.04	5.74	5.5
65.50	56.2	71.8	1.40	1110.0		105.0	112.1	35.1	9700	54000				83.4	0.97	5.31	5.5
67.50	57.3	64.3	1.57	1240.0		112.0	139.2	39.6	11600	67500				122.1	1.16	6.66	5.7
69.50	58.5	61.8	1.94	1190.0		131.0	182.5	54.2	15100	78000				168.5	1.51	7.69	5.1
72.50	60.2	68.8	1.36	1460.0		145.0	123.8	37.2	10000	59000				89.5	1.00	5.78	5.8
75.50	61.8	70.1	1.50	1550.0		158.0	114.9	36.2	9400	55000				72.7	0.94	5.37	5.7
77.50	63.0	68.8	1.31	1640.0		167.0	111.3	33.4	9500	55200				72.7	0.95	5.38	5.7
79.50	64.1	70.1	1.81	1520.0		181.0	106.6	35.8	9900	56300				72.9	0.99	5.48	5.5
82.50	65.8	73.9	1.22	1380.0		137.0	98.8	26.5	8600	47900				64.7	0.86	4.68	5.4
85.50	67.5	70.8	1.34	1360.0		149.0	116.8	47.4	8700	60300				79.2	0.87	5.91	6.8
87.50	68.6	71.2	1.49	1330.0		156.0	125.6	31.5	12000	54800				78.3	1.20	5.35	4.5
89.50	69.7	70.8	1.45	1420.0		158.0	126.7	40.6	9700	58800				80.9	0.97	5.75	5.9
92.50	71.2	69.8	1.54	1320.0		135.0	133.2	30.6	12100	60700				94.4	1.21	5.96	4.9

Depth (cm)	Age (kyr BP)	$CaCO_3$ (%)	Mo (ug/g)	Al (ug/g)	Ca (ug/g)	Ti (ug/g)	V (ug/g)	Cr (ug/g)	Mn (ug/g)	Fe (ug/g)	Ni (ug/g)	Cu (ug/g)	Zn (ug/g)	As (ug/g)	Mn (wt %)*	Fe (wt %)*	Fe/Mn (wt %)
95.50	72.6	68.8	1.50	1050.0		88.0	139.5	29.1	12600	60400				95.2	1.26	5.97	4.7
97.50	73.6	69.9	1.32	1160.0		164.0	104.2	18.1	11300	54700				88.9	1.13	5.34	4.7
102.00	75.8		1.63	1074.4	248052	114.0	148.9	22.9	13550	61001	91.7	261.2	133.3	94.1	1.35	6.01	4.4
105.50	77.5	63.9	2.33	1280.0		146.0	161.3	51.1	14000	75500				114.6	1.40	7.43	5.3
109.00	79.1		1.93	1200.2	250938	132.2	168.3	26.1	14717	69101	97.7	295.4	136.1	90.6	1.47	6.80	4.6
112.25	80.7		1.86	1200.3	225507	130.8	157.7	23.1	13738	66616	92.4	276.8	116.9	94.7	1.37	6.56	4.8
116.50	82.7	59.1	1.79	1460.0		135.0	166.9	28.6	14800	77300				124.1	1.48	7.62	5.2
124.25	86.5	65.9	1.90	1365.8	266830	146.4	158.4	21.8	13782	65355	85.7	287.8	117.8	83.7	1.38	6.42	4.7
127.00	87.8	71.6	1.72	1197.0	286551	148.5	126.6	18.8	11463	52982	79.4	236.9	103.5	53.3	1.14	5.18	4.5
129.00	88.8	71.4	1.62	1289.0	296221	158.5	127.8	15.8	11908	53975	79.2	249.9	105.9	53.3	1.19	5.27	4.4
130.50	89.5	66.8	1.59	1390.0		174.0	129.6	22.4	12300	63500				81.8	1.23	6.21	5.1
133.75	91.0	72.4	1.57	1259.4	297015	153.5	121.1	13.7	11579	51621	77.5	240.8	102.2	49.1	1.16	5.04	4.4
137.75	93.0	73.8	1.32	1190.8	270697	137.0	104.3	10.6	9804	42722	59.0	195.8	78.0	42.0	0.98	4.16	4.3
139.50	93.8	70.4	1.30	1420.0		140.0	114.1	15.9	11000	52300				63.0	1.10	5.12	4.7
142.00	95.0	74.0	1.30	1092.5	273536	145.2	103.4	13.2	9644	42550	63.8	199.0	82.2	42.5	0.96	4.14	4.3
147.00	101.3	72.7	1.53	1314.0	289649	149.2	124.2	14.5	11245	51612	69.9	244.5	110.2	50.8	1.12	5.04	4.5
150.50	105.6	72.8	1.34	1270.0		160.0	112.9	17.1	9900	50500				62.1	0.99	4.92	5.0
155.50	111.9	71.8	1.52	1314.2	287055	159.4	122.0	12.2	11620	52338	72.0	244.0	102.0	53.1	1.16	5.10	4.4
156.50	113.1	70.3	1.38	1500.0		150.0	119.1	14.7	11000	51900				61.1	1.10	5.07	4.6
158.25	115.1	56.4	2.27	1912.9	210671	239.9	169.6	21.2	15932	68715	93.2	339.7	137.6	74.4	1.59	6.68	4.2
162.00	116.6	67.4	2.25	1274.2	275497	138.1	178.6	16.8	17233	66329	94.2	342.2	130.0	90.0	1.72	6.52	3.8
168.75	119.4	66.3	2.30	1081.4	276750	118.0	197.6	15.3	19436	70855	92.6	376.1	146.9	100.2	1.94	6.99	3.6
174.00	121.5	60.2	2.98	870.4	241712	92.9	259.6	16.8	23477	88900	99.8	449.1	164.3	169.9	2.35	8.81	3.8
176.50	122.5	62.1	2.39	1060.0		263.0	225.0	18.9	20900	82300				140.3	2.09	8.02	3.8
182.75	125.0	57.0	2.65	929.8	220545	99.8	245.4	14.9	21527	86449	95.8	408.6	155.3	167.2	2.15	8.56	4.0
186.50	126.6	51.1	2.63	960.0		79.0	275.9	21.1	24400	109600				231.1	2.44	10.90	4.5

Depth (cm)	Age (kyr BP)	$CaCO_3$ (%)	Mo (ug/g)	Al (ug/g)	Ca (ug/g)	Ti (ug/g)	V (ug/g)	Cr (ug/g)	Mn (ug/g)	Fe (ug/g)	Ni (ug/g)	Cu (ug/g)	Zn (ug/g)	As (ug/g)	Mn (wt %)*	Fe (wt %)*	Fe/Mn (wt %)
191.75	128.7	59.7	2.49	1208.1	228989	117.6	208.6	12.4	18835	72920	90.7	319.6	139.9	129.6	1.88	7.20	3.8
194.50	129.8	64.2	2.62	1230.0		118.0	278.0	19.2	22300	107000				214.3	2.23	10.60	4.8
198.25	131.8	68.3	1.83	1243.1	269830	142.0	138.5	9.6	15201	60118	80.6	232.3	106.6	52.5	1.52	5.90	3.9
202.00	133.8	68.1	1.73	1237.6	268756	139.4	127.2	8.2	13117	55938	77.9	209.8	153.2	48.5	1.31	5.48	4.2
205.25	135.6	71.4	1.70	1215.5	282877	136.9	125.0	8.1	12884	54941	76.5	206.1	150.4	47.7	1.29	5.38	4.2
210.50	138.5	68.4	1.84	1370.0		120.0	107.7	11.1	15300	62000				74.9	1.53	6.10	4.0
215.50	141.2	71.5	1.53	1093.8	295119	123.2	112.5	7.3	11594	49441	68.9	185.4	135.4	42.9	1.16	4.84	4.2
225.50	146.6	70.4	1.42	1350.0		163.0	105.3	12.0	10700	58100				55.3	1.07	5.68	5.3
231.50	149.9	74.7	0.86	1659.0	295618	210.6	73.4	8.1	6536	40650	52.1	132.6	73.8	26.2	0.65	3.89	6.0
235.50	152.1	74.4	0.57	848.7	174118	115.2	48.6	9.0	3057	24679	26.1	78.0	41.2	17.2	0.30	2.37	7.8
235.50	152.1	75.6	0.84	1360.0		146.0	82.2	9.9	7300	46100				41.7	0.73	4.49	6.2
238.00	153.5	72.6	1.04	1510.6	284813	191.4	83.6	10.1	7332	44745	58.9	149.9	75.9	30.7	0.73	4.32	5.9
241.50	155.4	72.7	1.42	1576.8	281992	195.4	87.0	11.5	7227	46569	57.5	157.8	85.4	32.7	0.72	4.50	6.2
247.50	158.6	72.6	0.79	869.7	174072	112.2	56.1	7.8	5177	26672	47.6	95.9	61.7	20.4	0.52	2.58	5.0
250.50	160.3	73.3	0.83	715.9	174121	81.3	67.7	7.9	6126	28119	38.1	133.2	60.1	27.7	0.61	2.75	4.5
254.50	162.5	73.4	0.45	692.5	145894	78.4	38.3	3.7	3262	19438	22.1	73.1	31.4	14.3	0.33	1.88	5.8
258.50	164.6	75.2	0.86	744.3	230876	88.0	73.6	8.5	6644	30317	39.8	144.9	63.1	30.2	0.66	2.96	4.5

*Corrected for detrital Fe and Mn inputs

Table 4: Bulk sediment element concentrations from core OC73-03-20 (19°S).

Depth (cm)	Age (kyr BP)	$CaCO_3$ (%)	Mo (ug/g)	Al (ug/g)	Ca (ug/g)	Ti (ug/g)	V (ug/g)	Cr (ug/g)	Mn (ug/g)	Fe (ug/g)	Ni (ug/g)	Cu (ug/g)	Zn (ug/g)	As (ug/g)	Mn (wt %)*	Fe (wt %)*	Fe/Mn
4.0	5.4	41.1	44.85	2390.0	162896	373.8	532.9	53.1	55705	155768	289.3	960.5	361.6	290.4	5.57	15.58	2.7
8.0	7.8	26.2	47.90	1297.7	121985	196.3	623.6	60.1	59948	188467	266.2	1202.0	421.4	378.7	5.99	18.85	3.1
12.0	10.3	21.6	54.57	1121.2	99687	170.7	738.7	65.6	68802	227273	243.2	1607.7	525.5	450.0	6.88	22.73	3.3
16.0	12.7	15.5	53.09	862.7	76700	134.5	797.8	68.7	72121	247099	200.5	1614.3	525.5	493.5	7.21	24.71	3.4
20.0	15.1	12.2	56.98	781.3	67012	117.6	818.9	62.5	77004	246766	192.4	1623.4	588.3	495.5	7.70	24.68	3.2
24.0	17.6	14.7	53.94	913.6	71732	149.5	791.7	58.9	74412	242507	167.3	1478.1	633.2	507.2	7.44	24.25	3.2
28.0	20.0	8.0	54.02	646.3	50648	83.4	868.6	57.8	78591	264832	136.5	1719.8	687.0	518.1	7.86	26.48	3.4
32.0	21.4	35.1	29.22	1812.2	172160	284.4	361.0	19.8	42263	114221	237.5	559.6	271.9	209.8	4.23	11.42	2.6
36.0	22.8	44.3	28.34	2828.1	184235	428.0	352.7	23.6	40380	120857	278.3	539.1	257.2	219.8	4.04	12.09	2.9
40.0	24.1	45.5	24.24	3772.6	213093	561.4	326.8	27.4	34513	119347	256.1	455.5	204.3	199.3	3.45	11.93	3.3
44.0	25.5	45.5	23.19	3841.3	175508	554.8	334.8	28.9	31520	125631	251.1	441.3	192.0	210.3	3.15	12.56	3.8
48.0	26.9	37.7	31.21	3745.0	163193	531.1	468.8	34.4	40617	165722	289.1	595.6	246.7	314.0	4.06	16.57	4.0
52.0	28.3	33.4	36.26	2453.6	149789	338.7	566.4	30.4	46231	182717	262.2	696.4	303.5	348.3	4.62	18.27	3.9
56.0	29.7	42.0	31.70	2257.7	169807	328.8	410.8	18.4	36287	128357	209.4	511.4	231.5	250.2	3.63	12.84	3.5
61.0	31.4	47.6	25.76	2793.2	195292	458.0	360.5	16.5	34088	121134	230.7	484.4	214.3	205.0	3.41	12.11	3.4
66.0	33.1	46.6	28.42	3505.0	195962	572.3	391.1	19.0	37264	133003	238.3	541.1	230.9	229.7	3.73	13.30	3.5
70.0	34.5	43.4	31.33	4108.7	184886	692.9	421.2	20.9	40059	141702	254.6	580.3	254.7	253.1	4.01	14.17	3.4
74.0	35.9	42.4	28.30	4341.6	185279	678.6	387.5	19.9	37352	131492	224.7	534.6	239.8	216.8	3.74	13.15	3.4
78.0	37.3	39.3	32.77	4679.4	171866	666.5	453.6	22.5	40665	149618	227.6	617.6	281.5	264.4	4.07	14.96	3.6
82.0	38.7	42.1	30.84	4294.9	171966	598.5	450.2	23.2	42662	152423	239.8	654.7	282.1	270.1	4.27	15.24	3.5

*Corrected for detrital Fe and Mn inputs

Table 5: Bulk sediment element concentrations from core OC170-026-159 (39°S).

Depth (cm)	Age (kyr BP)	$CaCO_3$ (%)	Mo (ug/g)	Al (ug/g)	Ca (ug/g)	Ti (ug/g)	V (ug/g)	Cr (ug/g)	Mn (ug/g)	Fe (ug/g)	Ni (ug/g)	Cu (ug/g)	Zn (ug/g)	As (ug/g)	Mn (wt %)*	Fe (wt %)*	Fe/Mn
3.0	8.0	67.1	20.16	2032.7	294786	274.7	219.6	5.38	27542	67703	207.6	315.3	195.7	98.8	2.75	6.55	2.4
5.5	9.9	68.5	22.55	2043.9	283591	281.8	233.8	5.19	29320	70099	208.9	323.5	205.6	101.0	2.93	6.78	2.3
8.0	11.8		24.22	1968.9	267671	263.1	225.7	4.90	28921	69812	195.5	323.0	202.1	103.4	2.89	6.77	2.3
10.0	13.3	65.8	29.70	2009.6	273354	270.3	230.7	4.98	31504	74785	219.1	346.3	162.5	108.1	3.15	7.26	2.3
12.5	15.1		24.31	2115.3	277411	283.8	224.9	4.72	29610	71355	194.0	309.4	198.9	109.7	2.96	6.91	2.3
14.8	16.8	68.4	30.43	2235.1	280311	305.3	221.4	4.16	29267	72215	196.2	298.7	322.8	107.8	2.92	6.97	2.4
16.8	18.3		27.41	2380.6	286239	320.9	224.3	5.06	29575	72223	189.8	297.7	206.4	106.1	2.95	6.96	2.4
19.0	20.0	71.7	23.23	2689.5	286225	348.2	181.1	4.10	22555	62016	156.2	228.0	148.8	86.4	2.25	5.92	2.6
21.0	22.1		20.55	2614.9	299748	348.3	177.6	4.47	21736	59510	151.0	217.4	143.1	83.1	2.17	5.67	2.6
23.0	24.1	74.6	15.09	2966.6	314822	404.3	165.2	4.41	17658	57704	130.2	184.9	128.2	85.4	1.76	5.44	3.1
26.0	27.2		15.14	2759.8	309012	365.5	149.0	4.16	17802	52161	128.5	184.1	120.4	70.4	1.78	4.92	2.8
29.0	30.3	75.5	14.10	2938.3	326591	394.1	143.6	4.16	16535	50389	119.5	162.6	109.2	69.0	1.65	4.72	2.9
31.0	32.3		12.60	2814.8	306066	373.1	138.1	4.03	16262	49132	119.9	155.2	99.3	65.6	1.62	4.61	2.8
33.0	34.4	74.6	9.18	3280.3	326488	439.7	162.1	4.56	15693	57838	107.7	185.7	133.4	81.6	1.56	5.43	3.5
35.0	36.4		14.16	2882.0	319666	393.3	155.0	4.88	17655	54608	126.5	181.6	122.2	74.5	1.76	5.14	2.9
37.5	39.0	75.2	9.15	3227.2	325573	434.2	162.3	4.95	14929	58234	103.6	184.6	117.8	77.7	1.49	5.47	3.7
40.5	42.1		7.30	3075.0	309003	420.4	153.8	5.79	13628	54925	97.0	178.3	116.6	72.5	1.36	5.15	3.8
43.0	44.7	75.7	5.84	3614.7	319422	532.2	156.8	6.45	13603	59227	96.8	194.1	179.1	73.3	1.35	5.49	4.1
45.0	46.7		6.04	3196.1	302703	451.0	157.7	7.11	12713	56633	93.3	181.7	117.2	70.5	1.27	5.30	4.2
48.5	50.3	74.5	5.01	3238.3	318413	451.6	152.7	8.06	11774	56057	80.6	182.8	272.3	75.5	1.17	5.24	4.5
51.6	53.5		5.75	2816.1	321647	395.5	137.8	6.67	11077	48866	80.8	159.8	99.6	64.3	1.10	4.57	4.1
55.0	57.0	71.9	5.41	2802.7	300103	407.8	137.3	5.54	10994	49315	74.7	160.7	97.1	62.5	1.10	4.60	4.2
59.0	62.5		12.20	3140.2	325310	450.1	152.9	5.17	14538	52252	96.1	173.5	110.3	66.9	1.45	4.86	3.4
63.0	67.9	72.2	21.09	3557.8	295977	498.8	175.4	5.90	20647	58296	107.4	187.3	124.4	68.0	2.06	5.43	2.6
66.0	72.0		28.08	3589.6	305022	524.5	165.6	6.29	24473	54582	120.2	182.2	129.6	69.8	2.44	5.03	2.1

Depth (cm)	Age (kyr BP)	$CaCO_3$ (%)	Mo (ug/g)	Al (ug/g)	Ca (ug/g)	Ti (ug/g)	V (ug/g)	Cr (ug/g)	Mn (ug/g)	Fe (ug/g)	Ni (ug/g)	Cu (ug/g)	Zn (ug/g)	As (ug/g)	Mn (wt %)*	Fe (wt %)*	Fe/Mn (wt %)
68.0	74.0	72.9	7.49	3979.5	409973	632.3	134.7	6.40	12409	50224	87.4	150.9	88.5	58.8	1.23	4.51	3.7
70.0	76.0		7.56	4000.7	305171	608.0	126.7	6.76	11793	46722	78.2	151.1	89.5	52.0	1.17	4.18	3.6
72.3	78.3	74.4	12.96	4774.4	293635	750.3	165.8	7.57	17408	61543	116.1	198.4	125.1	66.1	1.73	5.55	3.2
74.8	80.8		10.54	4383.7	309493	595.6	139.7	6.67	14857	51443	127.7	178.6	102.4	57.1	1.48	4.66	3.2
77.0	83.0	73.6	9.93	3902.5	293149	526.4	137.3	7.38	14608	49691	121.3	187.3	99.9	57.9	1.46	4.54	3.1
79.0	85.0		15.37	4033.8	276144	488.9	168.9	5.28	18157	58537	141.2	235.3	123.4	71.1	1.81	5.46	3.0
81.5	87.5	68.9	14.79	4297.6	285189	530.4	180.2	6.65	19518	62032	151.5	254.7	132.2	75.0	1.95	5.77	3.0
84.3	90.3		17.94	4804.4	275898	553.4	195.4	6.38	21188	65834	160.4	268.3	143.9	82.7	2.11	6.14	2.9
87.0	93.0	68.8	16.12	5402.1	276592	557.5	198.6	7.90	22451	68575	162.8	282.7	148.5	82.0	2.24	6.41	2.9
89.8	95.8		12.53	5529.6	286613	555.8	165.5	5.90	18135	57025	130.9	225.7	125.8	65.0	1.81	5.25	2.9
92.0	98.0	70.4	15.78	6025.2	291208	589.2	179.5	7.10	21127	62284	163.5	261.8	142.8	70.8	2.11	5.75	2.7
94.0	100.0		17.62	4854.5	268980	491.0	181.5	8.29	19758	60847	153.3	255.6	136.1	74.7	1.97	5.69	2.9
96.0	102.0	66.9	20.49	5119.3	287270	537.9	198.5	8.54	23358	66589	178.4	293.7	157.8	84.7	2.33	6.22	2.7
98.0	104.0		19.43	4280.5	272023	486.6	201.8	7.22	21957	64218	166.0	279.7	147.2	80.3	2.19	6.03	2.8
100.5	106.5	63.9	22.39	4332.4	268250	508.1	221.4	20.74	22974	68298	192.4	299.8	152.8	87.0	2.29	6.42	2.8
103.0	109.0		21.72	4698.5	274776	598.1	237.5	6.18	23346	74823	179.2	316.2	167.7	97.3	2.33	7.00	3.0
105.5	111.5	63.3	23.04	4783.5	255837	599.2	242.4	12.30	23109	76907	164.4	319.4	164.7	104.8	2.30	7.21	3.1
108.0	114.0		15.67	5137.4	254592	661.5	208.9	8.91	21049	70633	149.7	290.3	197.1	86.8	2.10	6.53	3.1
109.5	115.5	62.0	12.66	7338.9	264742	1010.8	208.6	28.34	22090	77858	162.1	302.3	159.9	84.3	2.20	6.97	3.2
111.0	117.0		10.19	7982.8	240828	1173.6	173.8	11.03	19591	68861	141.9	266.7	146.9	70.6	1.95	5.94	3.0
113.5	119.3	60.5	10.95	8713.1	265578	1245.1	189.8	20.00	21138	75517	155.1	285.6	152.7	73.3	2.10	6.54	3.1
116.0	121.5		13.73	8223.3	230227	1160.4	180.0	10.74	22391	70953	171.0	289.7	155.6	68.9	2.23	6.16	2.8
118.5	123.8	52.0	19.05	8144.6	246319	1061.3	243.1	10.83	29572	88628	218.1	384.2	203.7	100.7	2.95	8.00	2.7
121.5	126.5		19.59	9394.9	213602	1849.9	220.0	13.29	28558	79871	172.7	335.3	209.8	82.5	2.84	6.49	2.3
124.5	130.3	38.3	10.43	22795.1	186353	4532.8	198.3	27.51	19630	82457	122.9	236.3	175.5	56.8	1.92	4.57	2.4
127.0	133.5		4.67	33161.3	165393	6865.9	220.0	48.60	10364	76857	76.1	124.4	133.5	31.0	0.97	2.12	2.2

Depth (cm)	Age (kyr BP)	$CaCO_3$ (%)	Mo (ug/g)	Al (ug/g)	Ca (ug/g)	Ti (ug/g)	V (ug/g)	Cr (ug/g)	Mn (ug/g)	Fe (ug/g)	Ni (ug/g)	Cu (ug/g)	Zn (ug/g)	As (ug/g)	Mn (wt %)*	Fe (wt %)*	Fe/Mn
129.5	136.8	34.6	2.87	42170.7	144998	7324.7	258.5	93.82	6570	79337	61.0	95.4	110.5	20.9	0.58	2.00	3.4
132.0	140.0		1.72	41234.4	153583	8218.6	241.0	50.52	4903	76595	48.9	86.8	104.2	16.0	0.41	1.00	2.5
132.0	140.0	35.1	2.27	32951.3	173860	5903.1	202.0	47.16	4972	64505	51.1	85.0	89.1	18.6	0.44	1.67	3.8
133.5	147.50		1.78	29761.2	201899	5257.8	191.5	44.01	5682	63640	50.4	89.3	87.9	24.3	0.52	2.11	4.1
134.5	152.50		2.00	19084.1	234996	3120.5	138.4	33.19	6533	52060	52.0	91.5	78.6	29.7	0.62	2.68	4.3
136.0	160.0		7.91	12197.0	403293	1955.6	148.1	17.52	12898	53734	92.4	155.6	108.6	49.8	1.27	3.79	3.0
138.5	190.5	55.6	28.91	3551.9	282149	559.3	223.8	9.15	29582	72508	194.1	310.3	189.6	98.1	2.95	6.80	2.3
141.0	201.7		30.61	22767.7	183658	2447.8	204.9	15.37	36980	83248	236.3	332.9	216.9	75.6	3.67	6.34	1.7
143.0	208.3	42.0	14.18	15871.7	160805	3029.3	156.6	16.54	23094	69714	176.2	250.2	164.5	52.4	2.28	4.52	2.0
145.0	215.0		13.22	18633.3	173620	3689.8	164.1	18.43	20753	71094	150.8	216.2	157.8	48.6	2.04	4.12	2.0
146.5	220.0	37.8	11.09	20823.3	157556	4073.5	164.4	22.86	18261	69252	133.6	205.3	150.0	44.8	1.79	3.63	2.0
148.0	225.0		8.23	30711.2	151956	5762.6	198.3	35.56	13750	73004	100.3	154.5	131.8	36.0	1.32	2.63	2.0
150.0	231.7	36.2	7.39	28598.2	142908	5665.0	186.7	30.29	12248	72266	91.3	144.4	123.6	35.0	1.17	2.64	2.3

*Corrected for detrital Fe and Mn inputs

Table 6: Mass accumulation rate fluxes (with error, see Methods) for Fe, Mn, and As (Y71-07-53, 11°S).

Depth (cm)	Age (kyr BP)	Fe flux (ug cm^{-2} yr^{-1})	Error (ug cm^{-2} yr^{-1})	Mn flux (ug cm^{-2} yr^{-1})	Error (ug cm^{-2} yr^{-1})	As flux (ug cm^{-2} yr^{-1})	Error (ug cm^{-2} yr^{-1})
0.25	19.5	70.84	11.41	23.47	3.77	0.13	0.02
0.75	19.8	78.88	12.72	22.50	3.62	0.12	0.02
1.75	20.4	63.23	10.23	21.57	3.48	0.11	0.02
3.25	21.2	61.04	9.85	20.34	3.28	0.09	0.02
4.25	21.8	58.52	9.45	15.62	2.52	0.09	0.01
5.25	22.3	57.71	9.27	13.20	2.12	0.08	0.01
6.75	23.2	52.75	8.46	11.42	1.83	0.08	0.01
8.25	24.0	49.81	7.95	11.27	1.80	0.08	0.01
9.25	24.6	53.99	8.66	9.59	1.54	0.09	0.02
10.25	25.1	54.75	8.73	12.68	2.02	0.09	0.01
11.75	26.0	59.80	9.60	10.07	1.61	0.08	0.01
13.25	26.8	63.88	10.29	13.05	2.10	0.10	0.02
14.25	27.4	59.57	9.61	14.89	2.40	0.11	0.02
15.25	28.0	53.59	8.64	12.75	2.05	0.09	0.01
16.75	28.8	57.56	9.28	14.52	2.34	0.10	0.02
18.25	29.6	32.32	5.17	6.82	1.09	0.06	0.01
19.25	30.2	52.50	8.42	12.91	2.07	0.08	0.01
20.25	30.8	57.23	9.17	13.30	2.13	0.09	0.01
22.50	32.0	52.44	8.39	14.45	2.31	0.09	0.01
25.50	33.7	56.99	9.19	15.10	2.43	0.10	0.02
27.50	34.8	56.05	8.97	13.99	2.24	0.09	0.01
29.50	36.0	61.07	9.78	11.55	1.85	0.09	0.02
32.50	37.7	64.05	10.31	11.39	1.83	0.11	0.02
35.50	39.3	53.26	8.55	10.10	1.62	0.09	0.01
37.50	40.5	62.39	10.06	13.42	2.16	0.12	0.02

Depth (cm)	Age (kyr BP)	Fe flux (ug cm^{-2} yr^{-1})	Error (ug cm^{-2} yr^{-1})	Mn flux (ug cm^{-2} yr^{-1})	Error (ug cm^{-2} yr^{-1})	As flux (ug cm^{-2} yr^{-1})	Error (ug cm^{-2} yr^{-1})
39.50	41.6	61.09	9.85	12.34	1.99	0.10	0.02
42.50	43.3	54.23	8.74	12.90	2.08	0.10	0.02
45.50	45.0	54.34	8.76	11.22	1.81	0.11	0.02
47.50	46.1	57.69	9.30	12.90	2.08	0.10	0.02
47.50	46.1	66.75	10.75	16.04	2.58	0.12	0.02
50.00	47.5	62.48	10.06	12.23	1.97	0.09	0.02
52.50	48.9	64.08	10.30	10.88	1.75	0.10	0.02
55.50	50.6	59.48	9.56	10.45	1.68	0.10	0.02
57.50	51.7	60.28	9.71	12.40	2.00	0.10	0.02
59.50	52.8	65.31	10.52	10.69	1.72	0.10	0.02
62.50	54.5	61.67	9.94	11.16	1.80	0.11	0.02
65.50	56.2	59.17	9.51	10.79	1.73	0.09	0.02
67.50	57.3	65.55	10.66	11.41	1.85	0.12	0.02
69.50	58.5	72.92	11.91	14.30	2.33	0.16	0.03
72.50	60.2	61.17	9.88	10.56	1.70	0.09	0.02
75.50	61.8	58.08	9.36	10.15	1.63	0.08	0.01
77.50	63.0	56.96	9.20	10.03	1.62	0.08	0.01
79.50	64.1	59.29	9.55	10.68	1.72	0.08	0.01
82.50	65.8	54.08	8.66	9.92	1.59	0.07	0.01
85.50	67.5	64.66	10.41	9.50	1.53	0.09	0.01
87.50	68.6	58.99	9.49	13.20	2.12	0.09	0.01
89.50	69.7	62.94	10.13	10.60	1.70	0.09	0.01
92.50	71.2	75.02	12.09	15.21	2.45	0.12	0.02
95.50	72.6	73.88	11.93	15.58	2.51	0.12	0.02
97.50	73.6	67.29	10.84	14.23	2.29	0.11	0.02
102.00	75.8	72.00	11.66	16.23	2.63	0.11	0.02

Depth (cm)	Age (kyr BP)	Fe flux (ug cm^{-2} yr^{-1})	Error (ug cm^{-2} yr^{-1})	Mn flux (ug cm^{-2} yr^{-1})	Error (ug cm^{-2} yr^{-1})	As flux (ug cm^{-2} yr^{-1})	Error (ug cm^{-2} yr^{-1})
105.50	77.5	85.07	13.85	16.01	2.60	0.13	0.02
109.00	79.1	76.70	12.51	16.58	2.70	0.10	0.02
112.25	80.7	71.49	11.70	14.97	2.45	0.10	0.02
116.50	82.7	81.24	13.34	15.76	2.58	0.13	0.02
124.25	86.5	75.82	12.30	16.27	2.64	0.10	0.02
127.00	87.8	67.18	10.80	14.85	2.38	0.07	0.01
129.00	88.8	68.11	10.95	15.37	2.47	0.07	0.01
130.50	89.5	74.38	12.05	14.71	2.38	0.10	0.02
133.75	91.0	66.33	10.65	15.22	2.44	0.06	0.01
137.75	93.0	56.21	9.00	13.22	2.12	0.06	0.01
139.50	93.8	65.06	10.48	13.97	2.25	0.08	0.01
142.00	95.0	56.03	8.97	13.04	2.09	0.06	0.01
147.00	101.3	25.67	4.12	5.72	0.92	0.03	0.00
150.50	105.6	25.09	4.03	5.04	0.81	0.03	0.01
155.50	111.9	25.59	4.11	5.82	0.93	0.03	0.00
156.50	113.1	24.75	3.99	5.36	0.86	0.03	0.00
158.25	115.1	81.26	13.41	19.36	3.19	0.09	0.02
162.00	116.6	93.59	15.14	24.71	3.99	0.13	0.02
168.75	119.4	98.50	15.97	27.37	4.43	0.14	0.02
174.00	121.5	113.24	18.55	30.15	4.93	0.22	0.04
176.50	122.5	105.90	17.29	27.57	4.50	0.19	0.03
182.75	125.0	105.14	17.33	26.42	4.35	0.21	0.03
186.50	126.6	123.61	20.60	27.67	4.61	0.26	0.04
191.75	128.7	91.82	15.06	24.02	3.93	0.17	0.03
194.50	129.8	144.61	23.53	30.39	4.94	0.29	0.05
198.25	131.8	63.75	10.30	16.42	2.65	0.06	0.01

Depth (cm)	Age (kyr BP)	Fe flux (ug cm^{-2} yr^{-1})	Error (ug cm^{-2} yr^{-1})	Mn flux (ug cm^{-2} yr^{-1})	Error (ug cm^{-2} yr^{-1})	As flux (ug cm^{-2} yr^{-1})	Error (ug cm^{-2} yr^{-1})
202.00	133.8	59.12	9.56	14.13	2.28	0.05	0.01
205.25	135.6	61.39	9.87	14.68	2.36	0.05	0.01
210.50	138.5	66.14	10.69	16.57	2.67	0.08	0.01
215.50	141.2	55.35	8.90	13.23	2.12	0.05	0.01
225.50	146.6	63.63	10.25	11.97	1.93	0.06	0.01
231.50	149.9	47.06	7.53	7.87	1.26	0.03	0.01
235.50	152.1	28.58	4.57	3.67	0.59	0.02	0.00
235.50	152.1	55.24	8.83	8.96	1.43	0.05	0.01
238.00	153.5	50.31	8.07	8.52	1.37	0.04	0.01
241.50	155.4	52.51	8.43	8.41	1.35	0.04	0.01
247.50	158.6	30.00	4.81	6.02	0.96	0.02	0.00
250.50	160.3	32.39	5.19	7.22	1.16	0.03	0.01
254.50	162.5	22.21	3.56	3.84	0.62	0.02	0.00
258.50	164.6	36.15	5.78	8.10	1.29	0.04	0.01

Table 7: Mass accumulation rate fluxes (with error, see Methods) for Fe, Mn, and As (OC170-026-159, 39°S).

Depth (cm)	Age (kyr BP)	Fe flux (ug cm^{-2} yr^{-1})	Error (ug cm^{-2} yr^{-1})	Mn flux (ug cm^{-2} yr^{-1})	Error (ug cm^{-2} yr^{-1})	As flux (ug cm^{-2} yr^{-1})	Error (ug cm^{-2} yr^{-1})
3.0	8.0	47.14	26.33	19.81	11.06	0.07	0.04
5.5	9.9	48.83	27.27	21.09	11.78	0.07	0.04
8.0	11.8	48.73	27.22	20.80	11.62	0.07	0.04
10.0	13.3	52.27	29.19	22.66	12.66	0.08	0.04
12.5	15.1	49.72	27.77	21.30	11.89	0.08	0.04
14.8	16.8	50.21	28.05	21.05	11.76	0.08	0.04
16.8	18.3	50.13	28.00	21.27	11.88	0.08	0.04
19.0	20.0	42.62	23.80	16.21	9.05	0.06	0.03
21.0	22.1	29.78	16.63	11.40	6.37	0.04	0.02
23.0	24.1	28.60	15.97	9.26	5.17	0.04	0.03
26.0	27.2	25.85	14.44	9.33	5.21	0.04	0.02
29.0	30.3	24.80	13.85	8.67	4.84	0.04	0.02
31.0	32.3	24.23	13.53	8.52	4.76	0.03	0.02
33.0	34.4	28.52	15.93	8.22	4.59	0.04	0.02
35.0	36.4	27.02	15.09	9.26	5.17	0.04	0.02
37.5	39.0	28.75	16.06	7.82	4.37	0.04	0.02
40.5	42.1	27.07	15.12	7.14	3.99	0.04	0.02
43.0	44.7	28.85	16.11	7.12	3.98	0.04	0.02
45.0	46.7	27.84	15.55	6.66	3.72	0.04	0.02
48.5	50.3	27.53	15.38	6.16	3.44	0.04	0.02
51.6	53.5	23.99	13.40	5.80	3.24	0.03	0.02
55.0	57.0	24.17	13.50	5.75	3.21	0.03	0.02
59.0	62.5	19.25	10.75	5.74	3.21	0.03	0.01
63.0	67.9	21.49	12.00	8.16	4.55	0.03	0.02
66.0	72.0	19.93	11.13	9.67	5.40	0.03	0.02

Depth (cm)	Age (kyr BP)	Fe flux (ug cm^{-2} yr^{-1})	Error (ug cm^{-2} yr^{-1})	Mn flux (ug cm^{-2} yr^{-1})	Error (ug cm^{-2} yr^{-1})	As flux (ug cm^{-2} yr^{-1})	Error (ug cm^{-2} yr^{-1})
68.0	74.0	24.36	13.60	6.67	3.72	0.03	0.02
70.0	76.0	22.57	12.61	6.34	3.54	0.03	0.02
72.3	78.3	29.95	16.73	9.36	5.23	0.04	0.02
74.8	80.8	25.17	14.06	7.99	4.46	0.03	0.02
77.0	83.0	24.53	13.70	7.86	4.39	0.03	0.02
79.0	85.0	29.47	16.46	9.78	5.46	0.04	0.02
81.5	87.5	31.18	17.41	10.51	5.87	0.04	0.02
84.3	90.3	33.13	18.50	11.41	6.37	0.04	0.02
87.0	93.0	34.59	19.32	12.09	6.75	0.04	0.02
89.8	95.8	28.36	15.84	9.76	5.45	0.04	0.02
92.0	98.0	31.06	17.35	11.38	6.35	0.04	0.02
94.0	100.0	30.71	17.15	10.64	5.94	0.04	0.02
96.0	102.0	33.61	18.77	12.58	7.03	0.05	0.03
98.0	104.0	32.55	18.18	11.83	6.61	0.04	0.02
100.5	106.5	34.66	19.36	12.38	6.91	0.05	0.03
103.0	109.0	37.79	21.11	12.57	7.02	0.05	0.03
105.5	111.5	38.91	21.73	12.45	6.95	0.06	0.03
108.0	114.0	35.25	19.69	11.33	6.33	0.05	0.03
109.5	115.5	37.62	21.01	11.87	6.63	0.05	0.03
111.0	117.0	32.05	17.90	10.52	5.87	0.04	0.02
113.5	119.3	38.87	21.71	12.48	6.97	0.04	0.02
116.0	121.5	36.56	20.42	13.23	7.39	0.04	0.02
118.5	123.8	47.54	26.55	17.50	9.77	0.06	0.03
121.5	126.5	38.54	21.53	16.85	9.41	0.05	0.03
124.5	130.3	19.00	10.61	7.97	4.45	0.02	0.01
127.0	133.5	8.82	4.93	4.02	2.24	0.01	0.01

Depth (cm)	Age (kyr BP)	Fe flux (ug cm^{-2} yr^{-1})	Error (ug cm^{-2} yr^{-1})	Mn flux (ug cm^{-2} yr^{-1})	Error (ug cm^{-2} yr^{-1})	As flux (ug cm^{-2} yr^{-1})	Error (ug cm^{-2} yr^{-1})
129.5	136.8	8.31	4.64	2.42	1.35	0.01	0.00
132.0	140.0	4.16	2.33	1.70	0.95	0.01	0.00
132.0	140.0	6.93	3.87	1.82	1.02	0.01	0.00
133.5	147.50	8.74	4.88	2.14	1.20	0.01	0.01
134.5	152.50	11.13	6.21	2.58	1.44	0.01	0.01
136.0	160.0	4.09	2.29	1.37	0.77	0.01	0.00
138.5	190.5	4.08	2.28	1.77	0.99	0.01	0.00
141.0	201.7	10.27	5.74	5.95	3.32	0.01	0.01
143.0	208.3	7.32	4.09	3.69	2.06	0.01	0.00
145.0	215.0	6.68	3.73	3.30	1.84	0.01	0.00
146.5	220.0	5.87	3.28	2.89	1.62	0.01	0.00
148.0	225.0	4.27	2.38	2.13	1.19	0.01	0.00
150.0	231.7	4.27	2.39	1.89	1.06	0.01	0.00

REFERENCES

Baker, E. T. (2009), Relationships between hydrothermal activity and axial magma chamber distribution, depth, and melt content, *Geochim. Geophys. Geosyst., 10*, Q06009, doi:10.1029/2009GC002424.

Baker, E. T., German, C. R. (2004), On the global distribution of hydrothermal vent fields, *in Mid-Ocean Ridges: Hydrothermal Interactions Between the Lithosphere and Oceans*, German, C. R., Lin, J., Parson, L. M., Eds. (Geophysical Monograph Series vol. 148, American Geophysical Union, 2004) pp. 245-266.

Baker, E. T., Chen, Y. J., Phipps Morgan, J. (1996), The relationship between near-axis hydrothermal cooling and the spreading rate of mid-ocean ridges, *Earth Planet. Sci. Lett.*, *142*, 137-145.

Bard, E., Hamelin, B., Fairbanks, R. G. (1990), U-Th ages obtained by mass spectrometry from corals from Barbados: Sea level during the past 130,000 years, *Nature*, *346*, 456-458.

Barreyre, T., Soule, S. A., Sohn, R. A. (2011), Dispersal of volcaniclasts during deep-sea eruptions: Settling velocities and entrainment in buoyant seawater plumes, *J. Volcanol. Geotherm. Res.*, *205*, 84-93.

Beaulieu, S.E., Baker, E.T., German, C.R., Maffei, A. (2013), An authoritative global database for active submarine hydrothermal vent fields, *Geochem. Geophys. Geosyst.*, *14*, 4892-4905.

Boström, K., Peterson, M. N. A., Joensuu, O., Fisher, D. E. (1969), Aluminum-poor ferromanganoan sediments on active oceanic ridges, *J. Geophys. Res.*, *74*, 3261-3270.

Burley, J. M. A., Katz, R. F. (2015), Variations in mid-ocean ridge CO_2 emissions driven by glacial cycles, *Earth Planet. Sci. Lett.*, *426*, 246-258.

Cartigny, P., Pineau, F., Aubaud, C., Javoy, M. (2008), Towards a consistent mantle carbon flux estimate: Insights from volatile systematics (H_2O/Ce, δD, CO_2/Nb) in the North Atlantic mantle (14°N and 34°N), *Earth Planet. Sci. Lett.*, *265*, 672-685.

Cave, R. R., German, C. R., Thomson, J., Nesbitt, R. W. (2002), Fluxes to sediments underlying the rainbow hydrothermal plume at 36°14′N on the Mid-Atlantic Ridge, *Geochim. Cosmochim. Acta.*, *66*, 1905-1923.

Clague, D. A., Paduan, J. B., Davis, A. S. (2009), Widespread strombolian eruptions of mid-ocean ridge basalt, *J Volcanol. Geotherm*. Res., *180*,171-188.

Clark, P. U., Dyke, A. S., Shakun, J. D., Carlson, A.E., Clark, J., Wohlfarth, B., Mitrovica, J. X., Hostetler, S. W., McCabe, A. M. (2009), The last glacial maximum, *Science*, *325*, 710-714.

Crowley, J. W., Katz, R. F., Huybers, P., Langmuir, C. H., Park, S. (2015), Glacial cycles drive variations in the production of oceanic crust, *Science*, *347*, 1237-1240.

Dunk, R. M., Mills, R. A. (2006), The impact of oxic alteration on plume-derived transition metals in ridge flank sediments from the East Pacific Rise, *Mar. Geol.*, *229*, 133-157.

Dymond, J. (1981), Geochemistry of Nazca plate surface sediments: An evaluation of hydrothermal, biogenic, detrital, and hydrogenous sources, *Geol. Soc. Am. Mem.*, *154*, 133-174.

Emerson, S., Hedges, J. I. (2004), Sediment diagenesis and benthic flux, *In: Treatise on geochemistry*. Turekian, H. D., Holland, H.D., Eds., p. 293.

Fairbanks, R. G., Mortlock, R. A., Chiu, T., Cao, L., Kaplan, A., Guilderson, T. P., Fairbanks, T. W., Bloom, A. L., Grootes, P. M., Nadeau, M. (2005), Radiocarbon calibration curve spanning 0 to 50,000 years BP based on paired $^{230}Th/^{234}U/^{238}U$ and ^{14}C dates on pristine corals, *Quaternary Sci. Rev., 24*,1781-1796.

Farley, K. A., Montanari, A., Coccioni, R. (2012), A record of the extraterrestrial ^{3}He flux through the Late Cretaceous, *Geochim. Cosmochim. Acta., 84*, 314-328.

Feely, R. A., Massoth, G. J., Baker, E. T., Lebon, G. T., Geiselman, T. L. (1992), Tracking the dispersal of hydrothermal plumes from the Juan de Fuca Ridge using suspended matter compositions, *J. Geophys. Res.-Sol. Ea., 97*, 3457-3468.

Francois, R., Frank, M., Rutgers van der Loeff, M. M., Bacon, M. P. (2004), ^{230}Th normalization: An essential tool for interpreting sedimentary fluxes during the Late Quaternary, *Paleoceanography, 19*, PA1018, doi:10.1029/2003PA000939.

Frank, M., Eckhardt, J., Eisenhauer, A., Kubik, P. W., Dittrich-Hannen, B., Segl, M., Mangini, A. (1994), Beryllium 10, thorium 230, and protactinium 231 in Galapagos Microplate sediments: Implications of hydrothermal activity and paleoproductivity changes during the last 100,000 years, *Paleoceanography, 9*, 559-578.

Froelich, P. N., Klinkhammer, G. P., Bender, M. L., Luedtke, N. A., Heath, G. R., Cullen, D., Dauphin, P., Hammond, D., Hartman, B., Maynard, V. (1979), Early oxidation of organic matter in pelagic sediments of the eastern equatorial Atlantic: suboxic diagenesis, *Geochim.Cosmochim. Ac., 43*, 1075-1090.

Gardeweg, M. C., Sparks, R. S. J., Matthews, S. J. (1998), Evolution of Lascar Volcano, Northern Chile, *J. Geol. Soc. London, 155*, 89-104.

German, C. R., Colley, S., Palmer, M. R., Khripounoff, A., Klinkhammer, G. P. (2002), Hydrothermal plume-particle fluxes at 13°N on the East Pacific Rise, *Deep Sea Research Part I: Oceanographic Research Papers*, *49*, 1921-1940.

Gregg, P. M., Hebert, L. B., Montési, L. G. J., Katz, R. F. (2012), Geodynamic models of melt generation and extraction at mid-ocean ridges, *Oceanography*, *25*, 78-88.

Haymon, R., Macdougall, D., Kastner, M., and Kerridge, J. (1979), Mineralogy and chemistry of hydrothermal sulfide deposits and sediments at EPR 21°N, *EOS, Trans., Am. Geophys. Union*, *60*, p. 864.

Hekinian, R., Fevrier, M., Bischoff, J. L., Picot, P., Shanks, W. C. (1980), Sulfide deposits from the East Pacific Rise near 21°N, *Science*, *207*, 1433-1444.

Hofmann, M., Morales Maqueda, M. A. (2009), Geothermal heat flux and its influence on the oceanic abyssal circulation and radiocarbon distribution, *Geophys. Res. Lett.*, *36*, L03603, doi:10.1029/2008GL036078.

Huybers, P., Langmuir, C. (2009), Feedback between deglaciation, volcanism, and atmospheric CO_2, *Earth Planet. Sci. Lett.*, *286*, 479-491.

Jellinek, A. M., Manga, M., Saar, M. O. (2004), Did melting glaciers cause volcanic eruptions in eastern California? Probing the mechanics of dike formation, *J. Geophys. Res.*, *109*, B09206, doi:10.1029/2004JB002978.

Jull, M., McKenzie, D. (1996), The effect of deglaciation on mantle melting beneath Iceland, *J. Geophys. Res.-Sol. Ea.*, *101*, 21815-21828.

Kelemen, P. B., Hirth, G., Shimizu, N., Spiegelman, M., Dick, H. J. (1997), A review of melt migration processes in the adiabatically upwelling mantle beneath oceanic spreading ridges, *Philos. T. Roy. Soc. A., 355,* 283-318.

Key. K., Constable, S., Liu, L., Pommier, A. (2013), Electrical image of passive mantle upwelling beneath the northern East Pacific Rise, *Nature, 495,* 499-502.

Lilley, M. D., Feely, R. A., and Trefry, J. H. (1995), Chemical and Biochemical Transformations in Hydrothermal Plumes, *Seafloor Hydrothermal Systems: Physical, Chemical, Biological, and Geological Interactions*, John Wiley & Sons, Ltd., 369-391.

Lisiecki, L. E., Raymo, M. E. (2005), A Pliocene-Pleistocene stack of 57 globally distributed benthic $\delta^{18}O$ records, *Paleoceanography*, *20,* PA1003, doi:10.1029/2004PA001071.

Lund, D. C., Asimow, P. D., Farley, K. A., Rooney, T. O., Seeley, E., Jackson, E. W., Durham, Z. M. (2016), Enhanced East Pacific Rise hydrothermal activity during the last two glacial terminations, *Science, 351,* 478-482.

Lund, D. C., Asimow, P. D. (2011), Does sea level influence mid-ocean ridge magmatism on Milankovitch timescales?, *Geochem. Geophys. Geosyst. 12,* Q12009, doi:10.1029/2011GC003693.

Lupton, J. (1998), Hydrothermal helium plumes in the Pacific Ocean, *J. Geophys. Res.-Sol. Ea.,103,* 15853-15868.

Lyle, M., (1992), Composition maps of surface sediments of the eastern tropical Pacific Ocean. *In* Mayer, L., Pisias, N., Janecek, T., et al., *Proc. ODP, Init. Repts.,* 138: College Station, TX (Ocean Drilling Program), 101–115, doi:10.2973/odp.proc.ir.138.108.1992.

Lyle, M. (1983), The brown-green color transition in marine sediments: A marker of the Fe(III)-Fe(II) redox boundary, *Limnol. Oceanogr.*, *28*, 1026-1033.

Maclennan, J., Jull, M., McKenzie, D., Slater, L., Grönvold, K. (2002), The link between volcanism and deglaciation in Iceland, *Geochem. Geophys. Geosyst.*, *3*, 1062, 10.1029/2001GC000282.

Marcantonio, F., Higgins, S., Anderson, R. F., Stute, M., Schlosser, P., Rasbury, E. T. (1998), Terrigenous helium in deep-sea sediments, *Geochim. Cosmochim. Acta.*, *62*, 1535-1543.

Marchig, V., Gundlach, H. (1982), Iron-rich metalliferous sediments on the East Pacific Rise: Prototype of undifferentiated metalliferous sediments on divergent plate boundaries, *Earth Planet. Sci. Lett.*, *58*, 361-382.

Metz, S., Trefry, J. H., Nelsen, T. A. (1988), History and geochemistry of a metalliferous sediment core from the Mid-Atlantic Ridge at 26°N. *Geochim. Cosmochim. Acta.*, *52*, 2369-2378.

Millero, F. Chemical Oceanography. Boca Raton: Taylor & Francis Group, LLC, 2013. (Chapter 10.2 – Hydrothermal Vent Chemistry)

Mills, R. A., Taylor, S. L., Pälike, H., Thomson, J. (2010), Hydrothermal sediments record changes in deep water oxygen content in the SE Pacific, *Paleoceanography*, *25*, PA4226, doi:10.1029/2010PA001959.

Morford, J. L., Emerson, S. (1999), The geochemistry of redox sensitive trace metals in sediments, *Geochim. Cosmochim. Acta*. *63*, 1735-1750.

Olive, J-. A., Behn, M. D., Ito, G., Buck, W. R., Escartín, J., Howell, S. (2015), Sensitivity of seafloor bathymetry to climate-driven fluctuations in mid-ocean ridge magma supply, *Science*, *350*, 310-313.

Palmer, M. R., Ernst, G. G. J. (1998), Generation of hydrothermal megaplumes by cooling of pillow basalts at mid-ocean ridges, *Nature*, *393*, 643-7.

Pollack, H. N., Hurter, S. J., Johnson, J. R. (1993), Heat flow from the Earth's interior: Analysis of the global data set, *Rev. Geophys.*, *31*, 267-280.

Richardson, C., McKenzie, D. (1994), Radioactive disequilibria from 2D models of melt generation by plumes and ridges, *Earth Planet. Sci. Lett.*, *128*, 425-437.

Schaller, T., Morford, J., Emerson, S. R., Feely, .R. A. (2000), Oxyanions in metalliferous sediments: Tracers for paleoseawater concentrations? *Geochim. Cosmochim. Ac.*, *63*, 2243-2254.

Schramm, B., Devey, C. W., Gillis, K. M., Lackschewitz, K. (2005), Quantitative assessment of chemical and mineralogical changes due to progressive low-temperature alteration of East Pacific Rise basalts from 0 to 9 Ma, *Chem. Geol.*, *218*, 281-313.

Shimmield, G. B., Price, N. B. (1988), The scavenging of U-^{230}Th and ^{231}Pa during pulsed hydrothermal activity at 20°S, East Pacific Rise, *Geochim. Cosmochim. Acta.*, *52*, 669-677.

Sigvaldason, G. E., Annertz, K., Nilsson, M. (1992), Effect of glacier loading/deloading on volcanism: Postglacial volcanic production rate of the Dyngjufjöll area, central Iceland, *B. Volcanol.*, *54*, 385-392.

Snoeckx, H., Rea, D. K. (1994), Late quaternary $CaCO_3$ stratigraphy of the eastern equatorial Pacific, *Paleoceanography*, *9*, 341-351.

Tolstoy, M. (2015), Mid-ocean ridge eruptions as a climate valve, *Geophys. Res. Lett.*, *42*, 1346-1351.

Tushingham, A. M, Peltier, W. R. (1991), Ice-3G: A new global model of Late Pleistocene deglaciation based upon geophysical predictions of post-glacial relative sea level change, *J. Geophys. Res.-Sol. Ea.*, *96*, 4497-4523.